

XMM-NEWTON AND GEMINI OBSERVATIONS OF EIGHT RASSCALS GALAXY GROUPS¹

ANDISHEH MAHDAVI

Institute for Astronomy, University of Hawaii

ALEXIS FINOGUENOV AND HANS BÖHRINGER

Max-Planck-Institut für Extraterrestrische Physik

MARGARET J. GELLER

Harvard-Smithsonian Center for Astrophysics

AND

J. PATRICK HENRY

Institute for Astronomy, University of Hawaii

Submitted September 30, 2004, accepted for publication in the Astrophysical Journal on December 8, 2004

ABSTRACT

We study the distribution of gas pressure and entropy in eight groups of galaxies belonging to the ROSAT All-Sky Survey / Center for Astrophysics Loose Systems (RASSCALS). We use archival and proprietary XMM-Newton observations, supplementing the X-ray data with redshifts derived from the literature; we also list 127 new redshifts measured with the Gemini North telescope. The groups are morphologically heterogeneous in both the optical and the X-ray, and several suffer from superpositions with background galaxies or clusters of galaxies. Nevertheless, they show remarkable self-similarity in their azimuthally averaged entropy and temperature profiles. The entropy increases with radius; the behavior of the entropy profiles is consistent with an increasing broken power law with inner and outer slope $0.92_{-0.05}^{+0.04}$ and $0.42_{-0.04}^{+0.05}$ (68% confidence), respectively. There is no evidence of a central, isentropic core, and the entropy distribution in most of the groups is flatter at large radii than in the inner region, challenging earlier reports as well as theoretical models predicting large isentropic cores or asymptotic slopes of 1.1 as $r \rightarrow \infty$. The pressure profiles are consistent with a self-similar decreasing broken power law in radius; the inner and outer slopes are $-0.78_{-0.03}^{+0.04}$ and $-1.7_{-0.3}^{+0.1}$, respectively. The results suggest that the larger scatter in the entropy distribution reflects the varied gasdynamical histories of the groups; the regularity and self-similarity of the pressure profiles is a sign of a similarity in the underlying dark matter distributions.

1. INTRODUCTION

Groups are the intermediate structures between galaxies and clusters of galaxies, and thus are crucial to an understanding of how galaxies evolve in dense environments (Zwicky 1937; Zwicky & Humason 1960; Hickson 1982; Geller & Huchra 1983; Ramella, Geller, & Huchra 1989; White et al. 1999). In the X-ray, groups and clusters are customarily distinguished by the temperature of the hot, gaseous medium that makes up $\approx 10\%$ of their total mass (Ebeling, Voges, & Böhringer 1994; Ponman et al. 1996; Mahdavi et al. 2000; Mulchaey 2000). Clusters, with temperatures $\gtrsim 2$ keV, contribute only about 3% to the matter density of the Universe; but groups, with X-ray temperatures in the range 0.5-2.0 keV (corresponding to a mass range 10^{13} - $10^{14} M_{\odot}$), contribute about twice as much (Ikebe et al. 2002; Reiprich & Böhringer 2002). Because of the cooler intracluster medium (ICM) temperature of the groups, the set of observable X-ray spectral lines is richer than it is in clusters, and allows a more accurate

determination of elemental abundances. The cD galaxies in groups make up a larger fraction of the total baryonic mass of the system than do the cD galaxies in clusters (Helsdon et al. 2001; Lin & Mohr 2004); hence the properties of the gaseous medium are more directly affected by the formation and evolution of the central galaxy. Finally, because the typical velocities of galaxies in groups are comparable to the galaxies' internal (stellar) velocity dispersions, galaxy interactions through the merging instability are common and very effective (Diaferio et al. 1993; Ramella et al. 1994).

Recent studies suggest that in the X-ray, the distinction between groups and clusters goes beyond an arbitrary temperature or mass boundary. Differences in the physical state of the intragroup medium make it difficult to view the $\lesssim 2$ keV systems simply as smaller, "rescaled" versions of the more massive clusters. Of particular interest are the heating of the ICM by nongravitational processes such as supernova explosions, stellar winds, AGN activity, and shocks resulting from interaction with the surround-

¹ Based on observations obtained with XMM-Newton, an ESA science mission with instruments and contributions directly funded by ESA Member States and the USA (NASA). The XMM-Newton project is supported by the Bundesministerium für Bildung und Forschung/Deutsches Zentrum für Luft- und Raumfahrt (BMFT/DLR), the Max-Planck Society and the Heidenhain-Stiftung, and also by PPARC, CEA, CNES, and ASI. Also based on observations obtained at the Gemini Observatory, which is operated by the Association of Universities for Research in Astronomy, Inc., under a cooperative agreement with the NSF on behalf of the Gemini partnership: the National Science Foundation (United States), the Particle Physics and Astronomy Research Council (United Kingdom), the National Research Council (Canada), CONICYT (Chile), the Australian Research Council (Australia), CNPq (Brazil), and CONICET (Argentina).

ing large scale structure (Ponman, Cannon, & Navarro 1999; Loewenstein 2001; Tornatore et al. 2003). Sometimes called “preheating,” these processes can leave a distinct mark on the entropy distribution of the gas in groups, to a degree not observable in more massive clusters. For this reason groups provide a fossil record of this energy production during cosmic structure formation and galaxy evolution.

In this study we focus on the distribution of entropy and pressure in eight systems drawn from the RASSCALs survey of nearby galaxy groups. In §2 and §3 we discuss the optical and X-ray data we have gathered for this study, as well as the data reduction procedures used in our analysis. In §4 we describe our attempts to fit self-similar profiles to the entropy and the pressure distribution. In §5 we describe each system in detail, In §6 we summarize our conclusions.

2. OPTICAL DATA

2.1. Sample Selection

At the focus of our study are groups with emission-weighted temperature $\sim 0.5 - 2$ keV. The X-ray luminosity-temperature relation (Ikebe et al. 2002) suggests that these groups should have $L_X \lesssim 10^{43}$ erg s $^{-1}$ in the 0.1-2.4 keV energy range.²

To build our sample, we begin with the ROSAT All-Sky Survey-Center for Astrophysics Loose Systems (RASSCALs), a statistically complete, magnitude-limited catalog of optically identified groups with $0.01 < z < 0.04$ (Mahdavi et al. 2000). This catalog contains 260 groups, of which 43 have X-ray emission detected in the RASS. To conduct a more detailed study of the properties of these groups, we select X-ray emitting RASSCALs with $L_X < 10^{43}$ erg s $^{-1}$ that have been observed with the XMM-Newton observatory. The properties of the sample are shown in Table 1.

The membership of the original RASSCALs groups was established spectroscopically with a completeness limit $m_R \approx 14.4$ (Ramella et al. 2002). All but one of the groups we have selected for analysis have also been the targets of deeper redshift surveys, by Mahdavi & Geller (2004) and Rines et al. (2003) (complete to $m_R \approx 15.4$), by Zabludoff & Mulchaey (1998) (70%–95% complete to different magnitude limits depending on the group), or by Pinkney et al. (1993) (unknown completeness). None of the groups had significant overlap with the current release of the Sloan Digital Sky Survey (Abazajian et al. 2004). In addition, we have performed optical observations which we describe below.

2.2. New Optical Spectroscopy

We observed three groups, RGH 80, HCG 97, and NRGb184 with the 8m Gemini North telescope on Mauna Kea, Hawaii. The Gemini multi-object spectrograph, GMOS, was used to measure redshifts for galaxies as faint as $m_R \approx 20$ within $6.5'$ of the center of each system.

The first step was the selection of targets for spectroscopy. We used GMOS in queue imaging mode to obtain a 2×2 , $13' \times 13'$ *R*-band mosaic around the central

galaxy in each group; the length of each imaging exposure was 10 minutes. The SExtractor package (Bertin & Arnouts 1996) then separated galaxies from stars, and calculated the magnitudes and half-light radii of the galaxies. It would have taken an inordinate amount of time to measure redshifts for all $m_R < 20$ galaxies in each image. Therefore, galaxies were sorted by their half-light radii, with the assumption that regardless of magnitude, galaxies with larger half-light radii would be more likely to have low redshifts and therefore belong to the group. All three groups are at a small enough redshift that foreground contamination was not an issue with this selection procedure.

In each piece of the mosaic, we selected the 20 galaxies with the largest half-light radii and without previously measured redshifts. Thus there were a total of 80 targets for NRGb184 and HCG 97. For RGH80, we included an additional central mask, for a total of 100 target galaxies. We designed one slit mask per image to be used with the GMOS B600 grating; the slit size was $0.5''$ (RGH80 and HCG 97) or $0.75''$ (NRGb184) achieving a resolution of $4 - 6 \text{ \AA}$ at 4000 \AA . The wavelength coverage was $4000 - 6000 \text{ \AA}$, with a shift of $0 - 1000 \text{ \AA}$ in either direction depending on the position of the galaxy on the focal plane. We used two 30 minute exposures per slit mask (a total of one hour), taking arc lamp exposures between each set of two exposures to obtain accurate wavelength calibrations. Because absolute photometric calibration is not required for redshift measurements, we did not apply flat-fielding or flux calibrations to the spectra.

The Gemini GMOS package for IRAF³ was used to calculate the wavelength solutions and to reduce the multi-object observations into one-dimensional spectra. The RVSAO package (Kurtz & Mink 1998), incorporating the methods of Tonry & Davis (1979), allowed us to measure redshifts by maximizing the cross-correlation of the spectra with absorption- and emission-line templates. The estimation of errors in the optical velocities is described in detail by Kurtz & Mink (1998), who determine the relationship between the shape of the cross-correlation function peak and the 68% velocity confidence interval using galaxies with known velocities. Our results are in Table 2.

2.3. Membership

We assemble a galaxy catalog by combining all the available redshift surveys in the direction of each group, and restricting ourselves to galaxies within 2 Mpc of the group center. The mean redshift z and velocity dispersion σ of each group are defined as follows (Danese, de Zotti, & di Tullio 1980):

$$z \equiv \frac{1}{N} \sum_{i=1}^N z_i; \quad (1)$$

$$\sigma^2 \equiv \sum_{i=1}^N \frac{(cz_i - cz)^2 - \epsilon_i^2}{(N-1)(1+z)^2}. \quad (2)$$

The subtraction of the root-mean-square velocity error in the second term is an attempt to remove the contribution of the measurement uncertainties ϵ_i to σ . In practice, this correction may be inaccurate when the underlying velocity distribution is nongaussian, the sample size is small

² We assume $H_0 = 70$ km s $^{-1}$ Mpc $^{-1}$, $\Omega_0 = 0.3$, and $\Omega_\Lambda = 0.7$ throughout the paper.

³ For a description of the Gemini data reduction package see <http://www.gemini.edu/sciops/data/dataSoftware.html>.

($N \lesssim 20$), and the velocity dispersion is of the same order of magnitude as ϵ_i . The inaccuracy is not a source of concern for our sample, but may be relevant for some extremely low-velocity dispersion groups with $\sigma \approx 70 \text{ km s}^{-1}$ (Mahdavi et al. 1999, 2000).

To determine group membership, we then use the “sigma-clipping” (Zabludoff, Huchra, & Geller 1990; Mahdavi & Geller 2004) algorithm to reject outliers, or galaxies unlikely to be bound to the group. This algorithm consists entirely of making sure that no group member is separated from its nearest neighbor in velocity space by more than the velocity dispersion σ of the group.

3. XMM-NEWTON OBSERVATIONS

We conducted XMM-Newton Observations of three of the eight groups, while the remaining five are publicly available in the XMM-Newton Data Archive. Table 3 contains the details of the observations.

The initial steps of the data reduction are similar to the procedure described in Zhang et al. (2004) and Finoguenov et al. (2003). The first important aspect is the removal of flares, which can significantly enhance the detector background, severely limiting the detection of low surface brightness features. Thus, for the group analysis, using flare free observing periods is critical. At energies above 10 keV the particle background dominates the detected counts; there is little X-ray emission from our targets because (1) the telescope efficiency is quite low at energies $> 10 \text{ keV}$, and (2) the temperature of the objects in our study is less than 2 keV. We use the 10–15 keV energy band (binned in 100s intervals) to monitor the particle background and to excise periods of high particle flux. In this screening process we use the settings FLAG=0 and PATTERN < 5 for the pn detector on XMM-Newton. We reject time intervals affected by flares by excising periods where the detector count rate exceeds the mean quiescent rate by more than 2σ . To produce the broad-band images and hardness ratio maps, we have also used the MOS1 and MOS2 events with PATTERN < 13 and FLAG=0. To reduce the widths of the gaps in the pn broad band images, we included photons near the pn-CCD borders, near bad pixels, and near offset columns. Data from the pn detector were used exclusively in the spectroscopic analysis described below.

Because most of the observations analyzed here were performed using a short integration frame time for pn (Full Frame Mode), it is important to remove the out-of-time events (OOTE) for accurate imaging and spectral analysis. We used the standard product of the XMMSAS 5.4 *epchain* task to produce the simulated OOTE file for all the observations and scale it by the fraction of the OOTE expected for the frame exposure time, (Table 3).

The cosmic component of the background consists of emission from the Galaxy as well as the extragalactic Cosmic X-ray Background (CXB). Observations of blank fields also contain both components. Provided that the exposures are done with the same instrumental set-up (e.g. with a particular filter) the spectra of the CXB are the same for both the target and the blank field. The Galactic component acts as an absorber and emitter, thus it is important to choose a similar absorbing column density for

both the target and background data sets, so that the expected background spectra are similar. In addition, there are variations in the Galactic emission on small scales.

The vignetting correction is performed taking into account the source extent, recent vignetting calibration (Lumb et al. 2004), and the pn response matrices released under XMMSAS 6.0. The residual systematic uncertainty of the flux is below 4% for the pn (Lumb et al. 2004).⁴

The analysis of each group consists of two steps: (1) construction of separate wavelet-decomposed maps of estimated surface brightness in the 0.5–2.0 keV band (I) and of emission-weighted temperature (T_I), which may be used to derive the entropy and pressure “integrated” along the line of sight; and (2) use of the wavelet-decomposed maps to identify contiguous regions from which we extract X-ray spectra for independent model-fitting.

The background-subtracted wavelet maps are based on photon images corrected for instrumental effects. The surface brightness map is constructed using the technique described in Vikhlinin et al. (1998). A hardness map of the emission then results from dividing the wavelet-reconstructed images in the 0.5–1 and 1–2 keV bands. The hardness ratio is a monotonic and unique function of the emission-weighted temperature, as long as the group redshift is well known (true for our sample). The advantages of using wavelets include the ability to remove additional background by spatial filtering and a control over the statistical significance of the detected structures. We use the “a trous” method of wavelet image reconstruction with scales from $8''$ to $4''$, applying a four sigma detection threshold and retaining emission to a 1.7σ detection limit. Occasionally, the wavelet algorithm generates small scale discontinuities in the reconstructed image. We remedy this effect by applying additional smoothing before producing the hardness ratio maps.

We also construct maps of the entropy and pressure “integrated” along the line of sight, using the surface brightness image and the emission-weighted temperature maps. The use of the word “integrated” is not strict, because these quantities do not have the dimensions of entropy or pressure times distance, and they serve as heuristic aids only. In studies of the intracluster medium, the common definitions of entropy and pressure are $kT/n^{2/3}$ and nkT , respectively, where n is the gas density and kT is the temperature in units of keV (see §4 for further details). Because the emission measure is proportional to n^2 , we use \sqrt{I} as an estimate of the gas density “integrated” along the line of sight. The “integrated” entropy is calculated simply as $T_I I^{-1/3}$, and the corresponding pressure as $\sqrt{IT_I}$. The quantities shown in these maps are not simply related to the physical, unprojected entropy and pressure, and they suffer from a number of degeneracies, with metallicity-density being the strongest (a significant fraction of the group emission results from line emission). Nevertheless, the maps indicate the regions of primary interest for further spectroscopic analysis, in which most of the degeneracies are removed. In general, we expect the entropy to increase monotonically with radius (Metzler & Evrard 1994), while the pressure should decrease. We stress that the “integrated” pressure and entropy are used only as tools to guide further spectroscopic analysis. They are

⁴ For further details of XMM-Newton processing we refer the reader to <http://wave.xray.mpe.mpg.de/xmm/cookbook/general>.

not used in the fits we discuss in §4.

The second, spectroscopic part of the analysis uses a mask file, constructed from both hardness ratio and surface brightness analysis described above. The first application of this technique is in Finoguenov et al. (2004). In our analysis we select regions with similar spectral properties. We combine the regions so that counting statistics are not the limiting factor in our derivation of the group properties. We use the wavelet-based maps to identify regions with similar X-ray colors and intensity levels. To generate the mask file for use in the further spectral analysis, we sample the changes in the intensity and hardness ratio at the precision allowed by the statistics of the data. We then examine each of the isolated regions with approximately equal color and intensity, imposing the additional criterion that the regions should be larger than the PSF width ($15''$) and contain more than 300 counts in the raw pn image. A sample mask file is shown in Figure 1.

The spectral analysis was performed using single-temperature models and the APEC plasma code, fitting elemental abundances from O to Ni as one group and assuming the photospheric solar abundance ratios of (Anders & Grevesse 1989). It should be noted that evidence for multiphase gas in groups of galaxies exists (Buote et al. 2003), such that gas at each *projected* radius may vary in temperature by a factor of ≈ 2 ; however, if the variations are due to a smooth radial trend in the plasma temperature (i.e., a temperature profile), a series of single-temperature fits across the group should roughly reproduce the general shape of the underlying pressure and entropy distributions.

In our analysis, we paid special attention to the issue of background estimation. We employ a double background subtraction technique, following Zhang et al. (2004). We used the region with radius 12–16' and 2–12 keV band to estimate the quality of the background subtraction using blank fields. This region is free of significant X-ray emission from the groups. We fix the shape of the residual background component, and also add a 0.2 keV thermal component (APEC with solar element abundance) to account for a possible variation in the Galactic foreground, allowing the normalizations of both components to be fit.

To estimate the true (as opposed to “integrated”) pressure nkT and entropy $kTn^{-2/3}$ in each region, we need measurements of both the gas density n and the temperature T . The spectral fit products, however, are kT and n^2V , where V is the volume of the emitting region. We do not have an exact knowledge of V . Because the mask generation technique identifies interesting regions by their wavelet-decomposed properties—producing region maps like Figure 1—a straightforward deprojection of the spectra is not possible. We therefore need to estimate the length of the column for each selected two-dimensional region on the sky. We assume that the gas emits uniformly along the line of sight as shown in Figure 2. With these approximations, the longest length through each volume is $L = 2\sqrt{R_2^2 - R_1^2}$, and the mean three dimensional distance of the region from the cluster center is $r = (R_1 + R_2)/2$. The volume of the region is then $2SL/3$, where S is the area of the region. A similar procedure is used in Henry, Finoguenov, & Briel (2004).

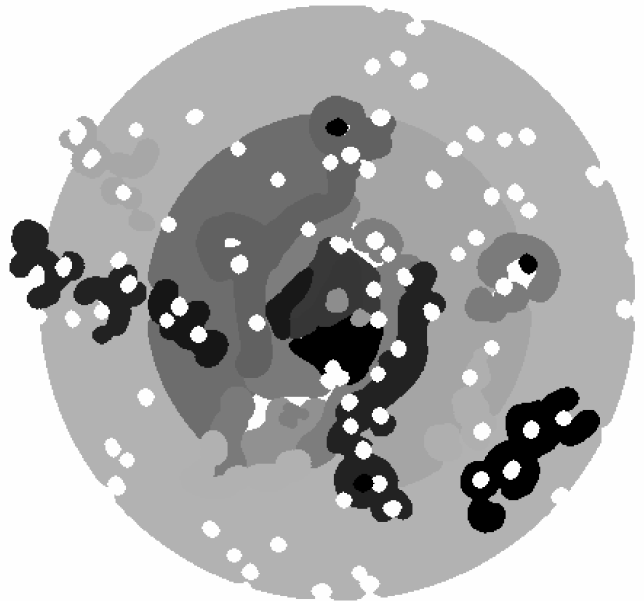


FIG. 1.— A sample extraction template for HCG 97. The spectra in each region are analyzed independently. White circles represent excised unrelated sources. In this particular image, darker colors represent higher emission-weighted plasma temperatures.

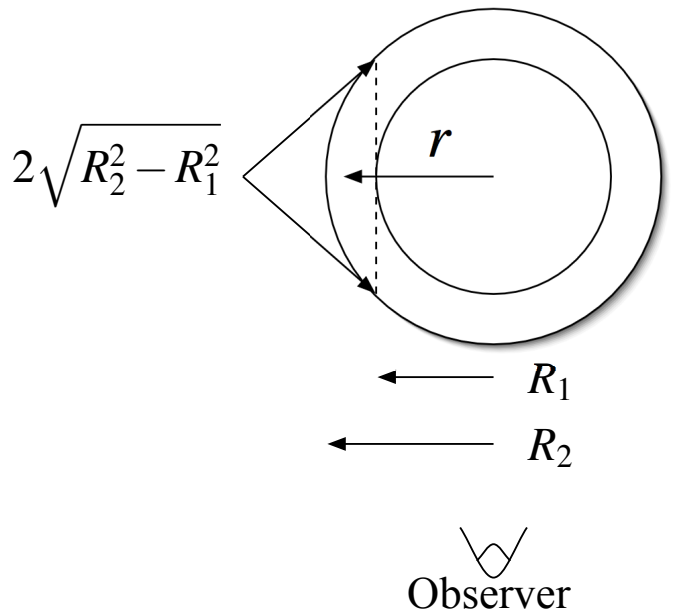


FIG. 2.— Simplification of the group geometry. The emitting region is to the left of the dashed line, and has a minimum and maximum projected distance R_1 and R_2 , respectively, from the group center. The distance along the line of sight is then $2\sqrt{R_2^2 - R_1^2}$.

Figures 3 and 4 show the gas density, temperature, entropy, and pressure distribution generated by the wavelet decomposition technique. The locations of the member galaxies also appear in these figures. Table 4 lists the basic physical properties of the X-ray emitting medium.

4. ENTROPY AND PRESSURE PROFILES

The distribution of entropy in systems of galaxies has been used to argue for the injection of “extra energy” into the intragroup medium during the formation process. Several authors (Ponman et al. 1999; Lloyd-Davies, Ponman, & Cannon 2000) have argued that in addition to

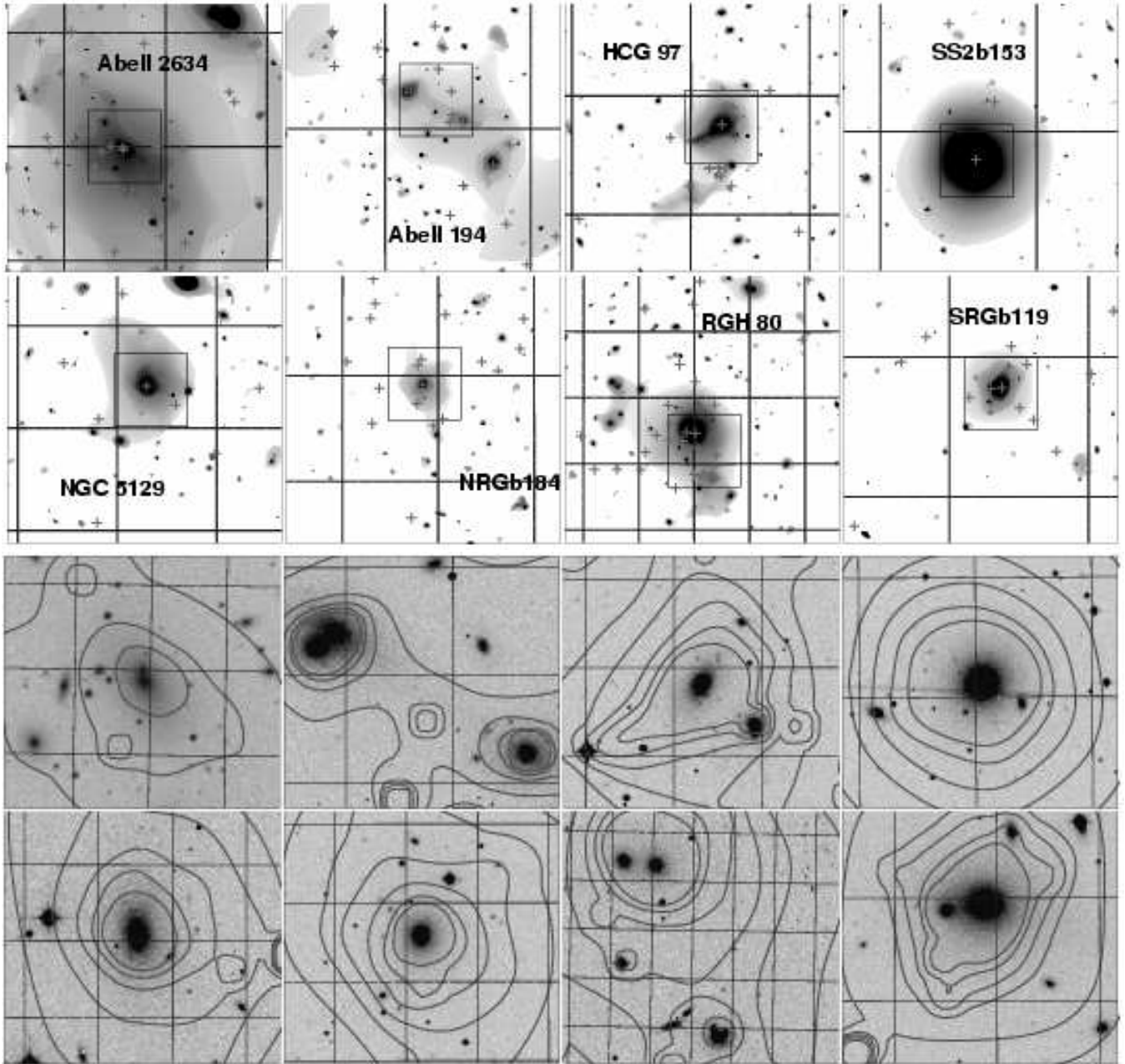


FIG. 3.— X-ray and optical images of the eight groups in our sample. (*Top*) Wavelet decomposition of the X-ray surface brightness in the 0.5-2.0 keV energy band. Each image is $19' \times 19'$; the grid cells are 200 kpc on a side. The small boxes show the area enlarged below. (*Bottom*) Palomar Observatory Sky Survey images of the central region of each group, with X-ray surface brightness contours superimposed from the above images. Each image is $5.2' \times 5.2'$ in size; the grid cells are 50 kpc on a side.

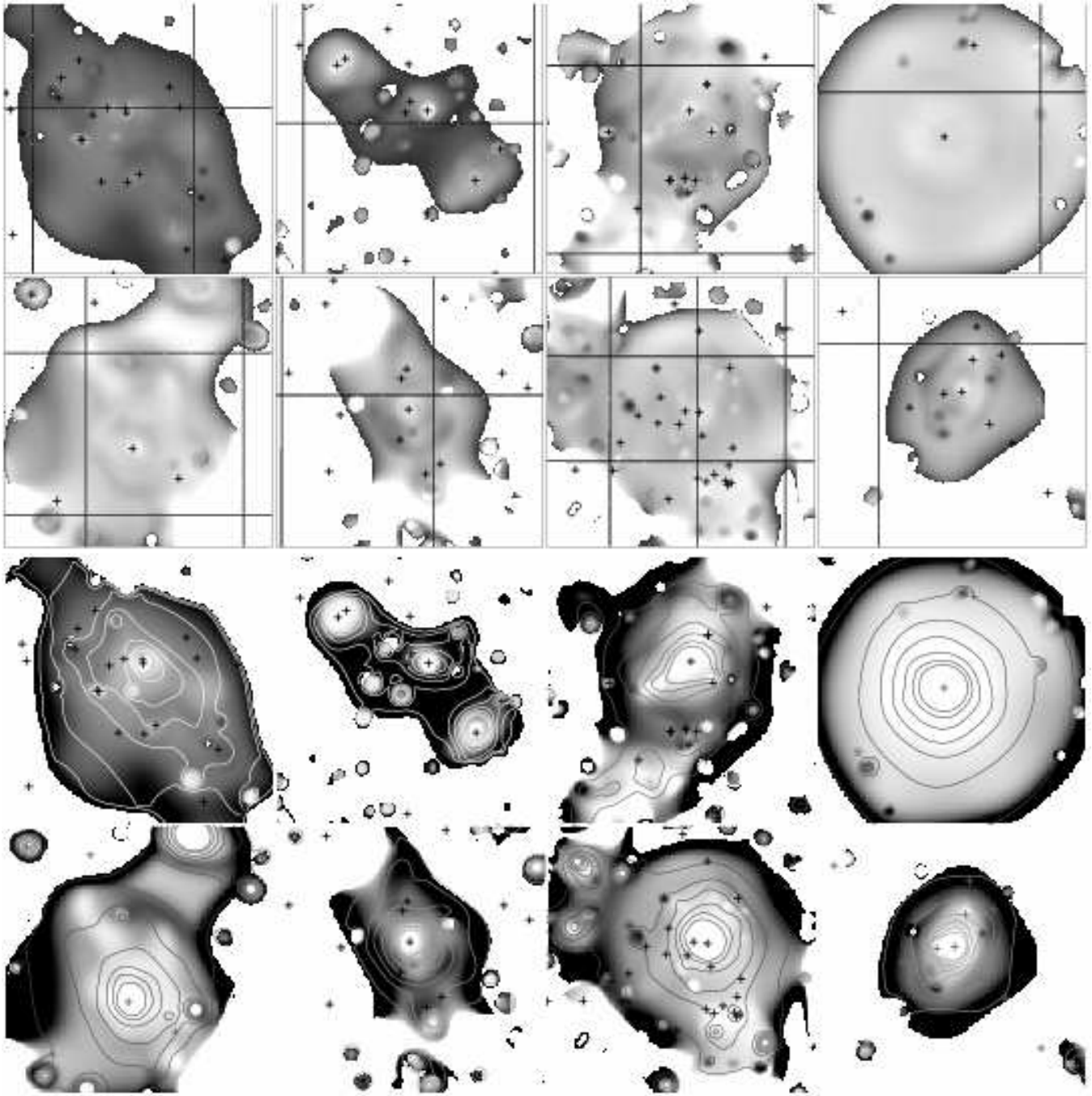


FIG. 4.— (*Top*) Emission-weighted temperature distribution of the sample from wavelet analysis. The range in temperatures shown is 0.5 keV (white) to 2.3 keV (black), with a linear scale. Member galaxies are shown as crosses. Each grid cell is 200 kpc on a side. (*Bottom*) Distribution of the entropy “integrated” along the sight, estimated from wavelet analysis. The range in integrated entropy shown is 10 (white) to 110 (black) in arbitrary units, with a linear scale. The contours show lines of constant gas pressure “integrated” along the line of sight; the innermost contours always show higher pressure, with each additional contour showing a decrement in pressure from the previous one of a factor of 1.5.

gravitational collapse, processes such as supernova explosions make a contribution to the thermodynamic state of the gas. This contribution takes the form of a “floor” in the inner entropy distribution of the intragroup medium as reported in these studies. In other words, gas with higher entropy than expected from pure gravitational collapse appears to be pooled at the center of groups observed by the ROSAT satellite. Ponman, Sanderson, & Finoguenov (2003) use a larger sample of 66 systems observed by ASCA to study this effect in greater detail. They find evidence of an entropy floor in these observations, with the notable exception that in lower temperature (less massive) systems the effect is much less pronounced than in higher temperature (more massive) ones. The entropy profiles of the less massive systems are better described by a simple power law.

Further complicating the picture, Finoguenov et al. (2002), using ASCA, found that gas at r_{500} (the radius within which the mean matter density is 501 times the critical density of the universe) also exhibits excess entropy relative to the pure gravitational value. This outer entropy excess seems consistent with models in which shock heating and galactic winds are also a major contributor to the groups’ dynamical evolution (Dos Santos & Doré 2002; Voit & Ponman 2003). In addition, Ponman et al. (2003) found that the entropy profiles, once scaled to $T^{0.65}$, are in agreement with each other, hinting at the possible universality of the entropy enrichment phenomenon. Some XMM-Newton observations are consistent with this result (Pratt & Arnaud 2002). Next we revisit all of these results.

4.1. Calculation of the Profiles

Figures 5 and 6 show the pressure and entropy as a function of true (as opposed to projected) distance from the center for our sample. The true distances were estimated not via deprojection but using the method described in §3 above. We define the gas entropy similarly to the earlier discussions of the intragroup medium (Ponman et al. 2003):

$$S \equiv Tn^{-\frac{2}{3}}, \quad (3)$$

where n is the particle number density and T is the temperature in keV. As a result, S has dimensions of keV cm². The traditional, thermodynamical entropy is then $\log S + C$, where C is an arbitrary constant.

We use the spectral fits discussed in §3 to plot the entropy as a function of distance from the cluster center. The fits are carried out in each region with the abundance, temperature, and gas density as free parameters, and with the hydrogen column fixed to the Galactic value from 21cm surveys (Dickey & Lockman 1990). The results are then used to calculate the entropy via equation (3). We add an additional 10% uncertainty to the entropy and pressure calculated in this manner to account for inaccuracies involved in our method of estimating distances from the center (§3); the volume estimates are more uncertain than the distances.

Because the entropy and pressure profiles in the groups appear similar, we test whether simple empirical models can describe their shapes, and whether the same entropy and pressure profiles can describe all the groups in our

sample. Rather than scaling the data by other derived values such as the temperature and r_{500} , we perform multidimensional fits (in up to 18 dimensions) as required to compare the data with the self-similar models.

4.2. Single Power Laws

To begin, we test whether the entropy and pressure profiles can be described by a single power law. From a theoretical point of view, such a profile seems unlikely, because N-body simulations (Navarro, Frenk, & White 1997; Ghigna et al. 2000) suggest that the mass distribution in dark haloes is not well fit by a single power law. The pressure and the entropy distribution depend on the temperature, and the temperature profile in turn depends on the overall matter density distribution. Thus it would be surprising if the resulting entropy and pressure were scale-free. However, noise may well make the observations consistent with a single power law, and it is important to test for this possibility before considering more complicated models.

We wish to discover whether the pressure and entropy distributions in our sample of groups are self-similar. Therefore, in fitting single power laws to the data, we constrain the slope of the power laws to be the same for all eight groups: $S(r) \propto r^{\mu_s}$ for the entropy, and $P(r) \propto r^{\mu_p}$ for the pressure. Each fit has 9 free parameters: one slope and eight normalizations. We minimize the χ^2 statistic via the built-in implementation of simulated annealing (Press et al. 1992) in the Sherpa data analysis package⁵. Simulated annealing is a compromise between downhill minimization (which is fast but may not always find a global minimum) and monte-carlo minimization (which is slow but has a greater likelihood of finding a global minimum).

The results appear in the top halves of Figures 5 and 6. The fits are not acceptable, yielding reduced χ^2 of 2.42 and 3.32 for the entropy and pressure data, respectively. We conclude that neither the entropy nor the pressure profiles are consistent with a single universal power law.

We can proceed either by treating the groups as individual entities—fitting independent single power laws to each system—or by considering more complicated universal models. The first approach yields an acceptable fit for the entropy profiles of Abell 2634 ($\mu_s = 0.21 \pm 0.10$), NGC 5129 ($\mu_s = 0.79 \pm 0.08$), HCG 97 ($\mu_s = 0.59 \pm 0.04$), RGH 80 ($\mu_s = 0.62 \pm 0.03$), SS2b153, ($\mu_s = 0.72 \pm 0.04$), and SRGb119 ($\mu_s = 1.1 \pm 0.1$); Abell 194 and NRGb184 do not yield acceptable fits. For the pressure profiles, single power laws yield a good fit to Abell 2634 ($\mu_p = -1.2 \pm 0.1$), NGC 5129 ($\mu_p = -1.0 \pm 0.1$), Abell 194 ($\mu_p = -0.92 \pm 0.11$), NRGb184 ($\mu_p = -0.73 \pm 0.05$), SS2b153 ($\mu_p = 1.26 \pm 0.04$), SRGb119 ($\mu_p = 1.1 \pm 0.09$); HCG 97 and RGH 80 are not consistent with a single power law. Interpreting these individual slopes is by no means straightforward, especially in light of the fact that we may not be sufficiently sampling the central regions of the more distant systems. It is far more instructive to consider whether a more detailed universal profile can describe all the data.

4.3. Broken Power Laws

⁵ Sherpa was used for fitting the radial profiles only; details on the software may be found at <http://asc.harvard.edu/sherpa/>

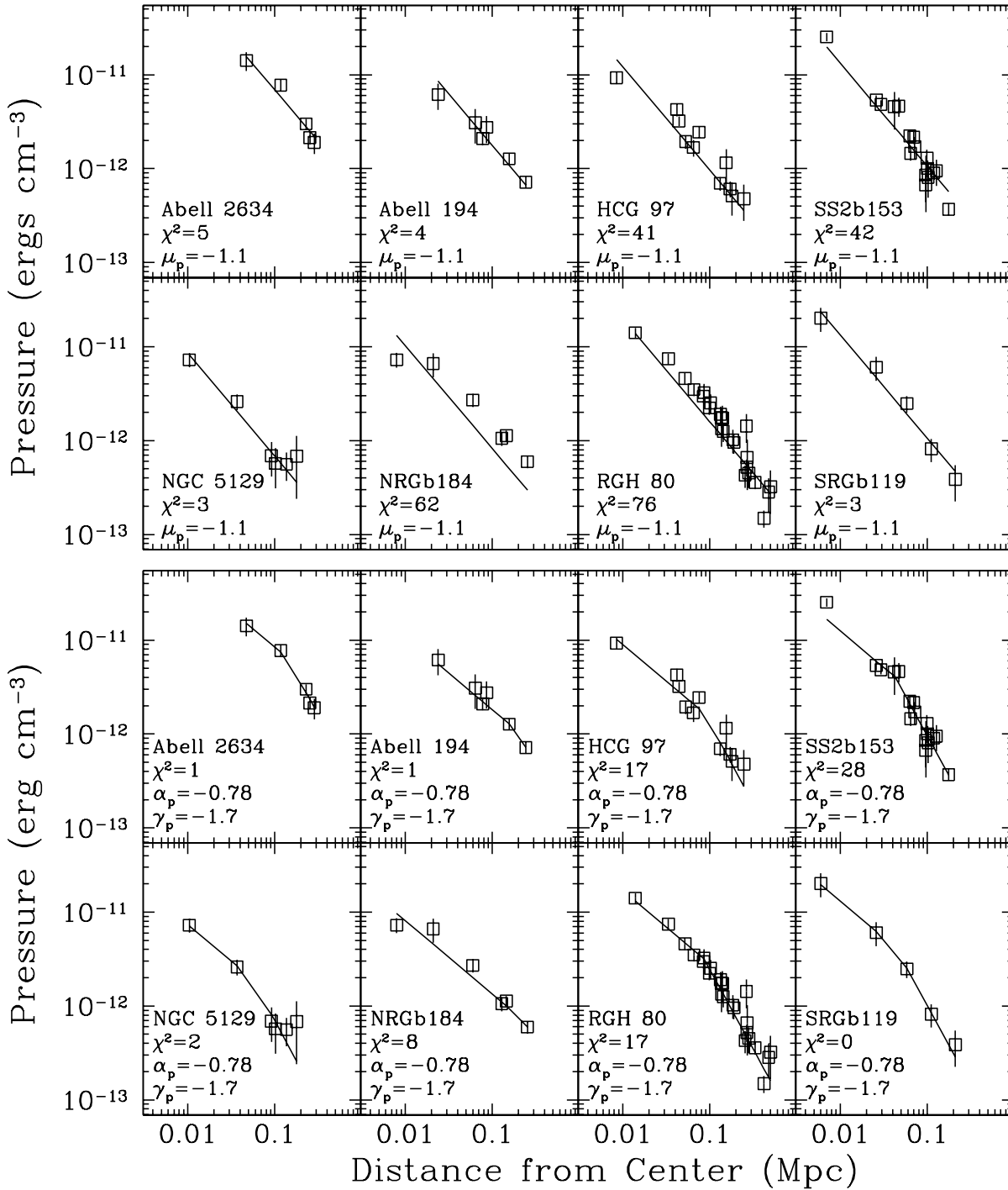


FIG. 5.— Pressure distributions for the eight groups in our sample. (*top*) Single-power law fit to the entire sample, with the slope constrained to be same for each group; the reduced χ^2 is 3.32. (*bottom*) Broken power law fit; the reduced χ^2 is 1.18.

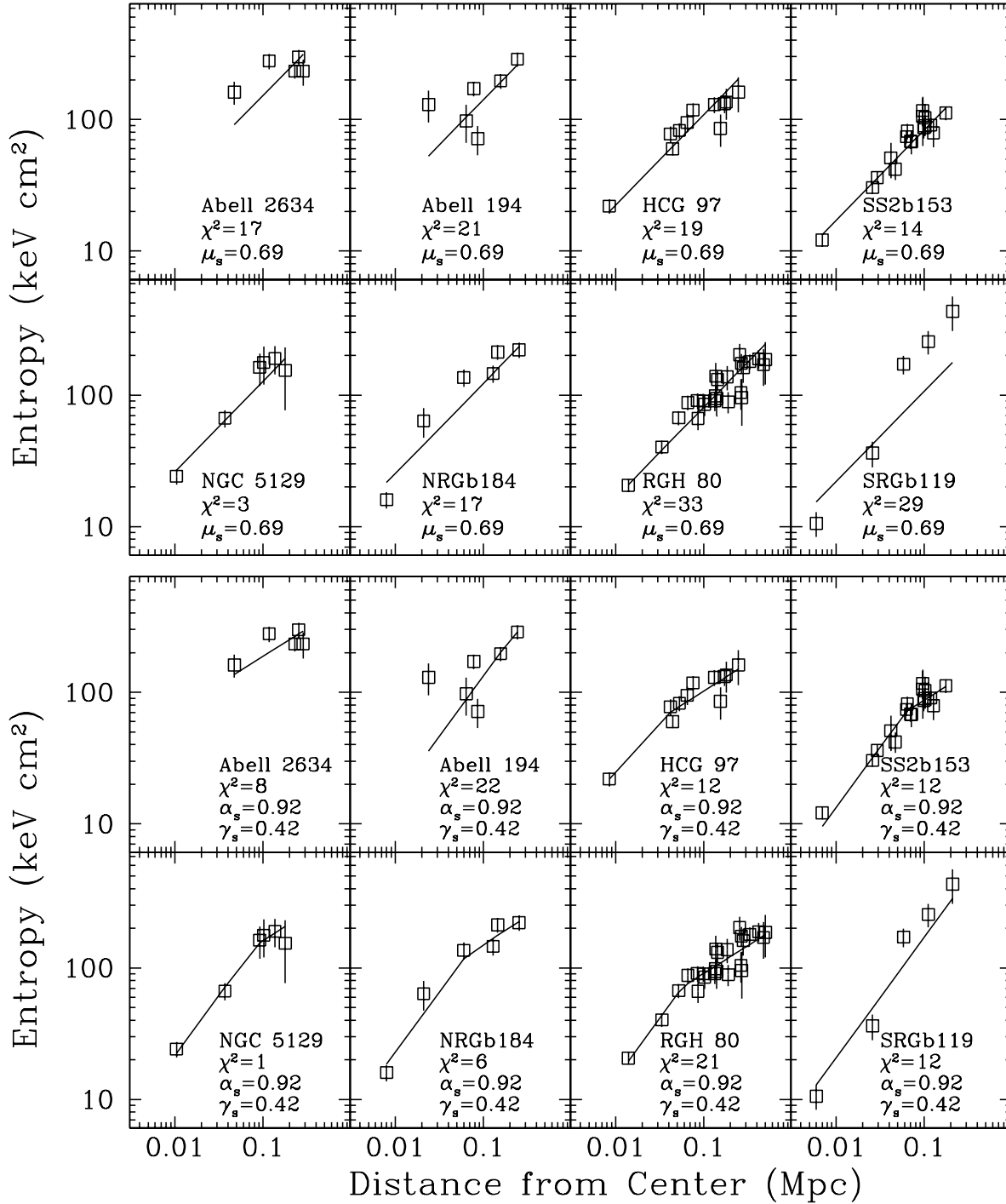


FIG. 6.— Entropy distributions for the eight groups in our sample. (*top*) Single-power law fit to the entire sample, with the slope constrained to be same for each group; the reduced χ^2 is 2.42. (*bottom*) Broken power law fit; the reduced χ^2 is 1.50.

We test the self-similarity of the entropy and pressure profiles by fitting broken power laws of the form

$$P(r) = P_0 \begin{cases} (r/100 \text{ kpc})^{\alpha_p} & r < r_p \\ (r_p/100 \text{ kpc})^{\alpha_p - \gamma_p} (r/100 \text{ kpc})^{\gamma_p} & r > r_p \end{cases} \quad (4)$$

Similarly, we fit entropy profiles of the form

$$S(r) = S_0 \begin{cases} (r/100 \text{ kpc})^{\alpha_s} & r < r_s \\ (r_s/100 \text{ kpc})^{\alpha_s - \gamma_s} (r/100 \text{ kpc})^{\gamma_s} & r > r_s \end{cases} \quad (5)$$

For these self-similar models we conduct two separate analyses: a pressure fit and an entropy fit. The pressure fit has 18 free parameters: the slopes α_p and γ_p common to all the groups, and eight different pairs (r_p, P_0) for each group. Similarly, the entropy fit has its own set of 18 parameters.

Minimizing χ^2 using the same technique as in the previous section yields good fits; these are shown in the bottom half of Figures 5 and 6. In Table 5, we estimate the goodness-of-fit (the probability of observing $\chi^2 > \chi_{\min}^2$ if the model is correct) as the definite integral of the χ^2 distribution, $q = \Gamma(\nu/2, \chi^2/2)/\Gamma(\nu/2)$, where $\Gamma(a, x)$ is the incomplete gamma function, $\Gamma(a) = \Gamma(a, 0)$ is the gamma function, and ν is the number of degrees of freedom (i.e., the number of data points minus the number of free parameters minus one).

After finding the minimum, we calculate errors on the best-fit parameters by using likelihood ratio tests (Lupton 1993). This method fully takes the correlations among the parameters into account. The test involves repeatedly comparing the overall minimum χ^2 with χ^2 minimized assuming many different fixed values for the parameter in question. The set of differences between the global minimum and the constrained minima has a χ^2 distribution with one degree of freedom asymptotically, and this fact may be used to estimate confidence intervals. For each parameter we re-minimize χ^2 100 times around the best-fit value; the error estimation procedure thus involved 1800 re-minimizations in all.

4.4. Results

We find that a broken power law provides a good description of the combined pressure profiles of the eight groups (see Table 5 and Figure 5). The pressure broken power law has a shallow slope $-0.78_{-0.03}^{+0.04}$ near the group center, steepening to $-1.7_{-0.3}^{+0.1}$ at the outer edges; the goodness-of-fit is an acceptable $q = 0.15$. The agreement is not perfect: NRGb184 is entirely consistent with a single, rather than a broken power law, and SS2b153 exhibits a somewhat steeper inner pressure profile than the other seven groups. Otherwise, the notion that the groups are self-similar systems differing only in a radius and absolute pressure scaling is supported by the XMM-Newton data.

The entropy profiles (Figure 6), however, make the picture more complicated. The broken power law fit to the combined data has fit quality $q = 0.0095$; the model is acceptable at 3σ . Excluding the binary cluster Abell 194 would bring the goodness-of-fit to a wholly acceptable $q = 0.136$, and would not affect the best-fit slopes substantially. The inner power law slope, $0.92_{-0.05}^{+0.04}$, is steeper than the outer entropy slope $0.42_{-0.04}^{+0.05}$, meaning there is no

evidence for an constant-entropy ‘‘floor’’ as close as 10 kpc from the center of each group. Rather, in contrast to previous observations with ROSAT and ASCA, the entropy profile shows a tendency to steepen towards the center of each group. There is an entropy deficit at larger radii relative to the extrapolation one would obtain from the inner power law, a new result not seen in data from the older X-ray observatories.

It is instructive to compare our data with theoretical models. Tozzi & Norman (2001) make detailed predictions for the entropy profiles of groups and clusters of galaxies in two different scenarios: with preheating (where a significant initial entropy excess exists in the systems at $t \approx 1$ Gyr), and without preheating (where the gas dynamics is chiefly determined by shocks and gravitational heating). In the first scenario, they find that more massive clusters develop isentropic cores within $\sim 0.05r_{200}$, and that less massive groups develop relatively larger cores (within $\sim 0.5r_{200}$). By contrast, in the scenario without preheating, groups and clusters both tend to develop power law entropy distributions, with $S(r) \propto r^{1.1}$.

To test these scenarios, we combine our entropy profiles in several ways (Figure 7). In (a), we show all the groups for which the preferred fit is a broken power law—that is, the groups for which r_s is neither a lower nor an upper limit. Here the radii are scaled by r_s , and the entropies by $S(r_s)$. As might be expected, this combination of profiles exhibits little scatter around the best-fit line, because the highest contributors to χ^2 —Abell 194 and SRGb119—are not included. In (b) we show the profiles for all eight groups, scaled by r_{500} and $\langle S \rangle$, the mean entropy within r_{500} as listed in Table 4. Despite the difference in scaling, the data are still well described by our best-fit broken power law with fixed slopes $\alpha_s = 0.92$ and $\gamma_s = 0.42$ —in fact, the fit quality is higher, because the additional uncertainty introduced through division by $\langle S \rangle$ decreases the reduced χ^2 . We compare these profiles with the predictions of the Tozzi & Norman (2001) preheating model, where we assume that $\langle S \rangle = S_\infty/2$, where S_∞ is the entropy of the last accreted gas shell. The model is rejected, because it predicts a large isentropic core that we do not observe and an outer profile that rises more quickly than ours. Varying $\langle S \rangle/S_\infty$ arbitrarily in either direction does not change this result. Finally, in (c) we show the eight groups again, with the radii scaled by r_{500} , but with the entropies scaled by $(T/\text{keV})^{0.65}$, a relation Ponman et al. (2003) derive for their sample of 66 virialized groups and clusters. This scaling agrees with our $\alpha_s = 0.92$ and $\gamma_s = 0.42$ fits as well, but is clearly inconsistent with both the preheated and non-preheated Tozzi & Norman (2001) models—both models are rejected with $q < 10^{-6}$.

Thus there are two key differences between our results and the Tozzi & Norman (2001) models: (1) we do not observe any isentropic cores, and (2) we find an entropy decrement at radii $\gtrsim 0.5r_{500}$ with respect to the extrapolation from data at radii $\lesssim 0.5r_{500}$. Neither of these results is unique to our sample: both effects are also clear in the high quality Chandra observation of the NGC 1550 group (Sun et al. 2003); the lack of an isentropic core is also clear in the Chandra and XMM-Newton observations of ESO 306170 (Sun et al. 2004) and in a few of the groups studied by Ponman et al. (2003). These stud-

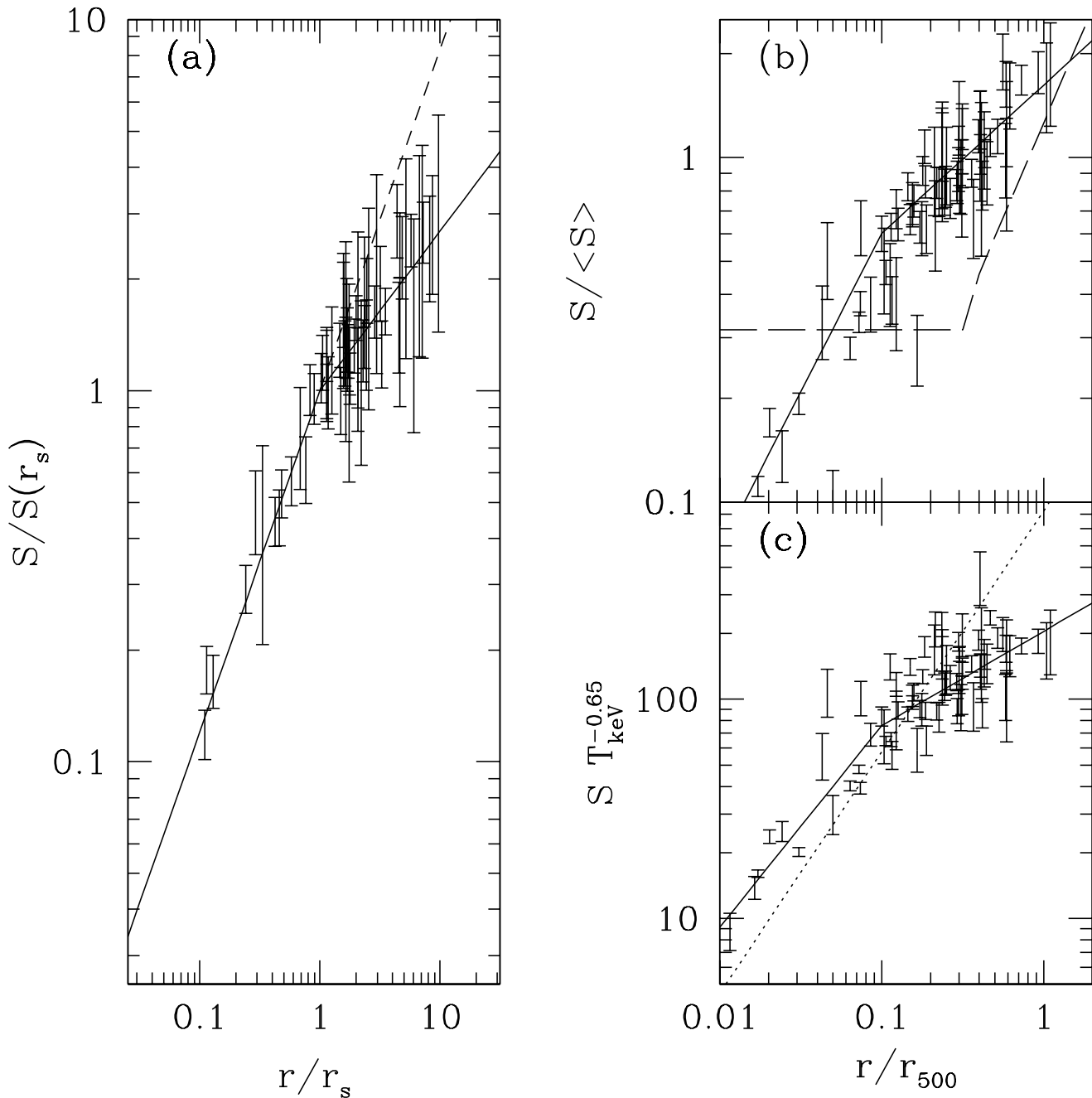


FIG. 7.— The entropy profiles combined using (a) our fit results, but leaving out groups where $S(r)$ is consistent with a single power law; (b) all groups, with the radii scaled by r_{500} and the entropies scaled by the mean entropy $\langle S \rangle$ within r_{500} ; and (c) all groups with the radii scaled by r_{500} and the entropies combined according to the scaling relation derived by Ponman et al. (2003). The solid curve in all three figures shows the broken power law derived from our analysis, $\alpha_s = 0.92$ and $\gamma_s = 0.42$, with the breaking radius and normalization adjusted to fit the data in (b) and (c). The short-dashed line in (a) shows the continuation of the $\alpha_s = 0.92$ power law. The long-dashed curve in (b) shows the prediction of the Tozzi & Norman (2001) preheating model. The dotted curve in (c) shows the (rejected) best-fit power law with slope fixed at 1.1.

ies employ deprojection techniques very different from our mask-based approach; thus it is unlikely that we are witnessing a peculiar effect due to the instrument or due to our data reduction technique.

In the inner regions, the disagreement with older studies may be due to the improved spatial resolution of Chandra and XMM-Newton. In studies such as Ponman et al. (2003), the distribution of the gas in groups is assumed to follow a single β -model distribution, with gas density $\rho_g \propto (1 + r^2/r_c^2)^{-3\beta/2}$ (Sanderson et al. 2003). Higher resolution data indicate, however, that the gas density rises more steeply towards the center due to the influence of the dominant central galaxy (Helsdon & Ponman 2000; Lewis, Buote, & Stocke 2003; Buote et al. 2003; Sun et al. 2003, 2004), with n better described by a broken power law or by two superposed β -models. In this scenario, as $r \rightarrow 0$, the entropy $S \propto T/n^{2/3}$ declines more rapidly than it does for an equivalent single β model, unless r_c is very small.

The disagreement with the theoretical models predicting large isentropic cores is likely related to the assumed equation of state of the gas. In such models (Tozzi, Scharf, & Norman 2000; Tozzi & Norman 2001), the initial gas density profile follows a polytropic distribution, $n \propto p^{1/\eta} \propto T^{1/(\eta-1)}$, with η being the adiabatic index. Given this functional relationship, the temperature gradient dT/dr is inevitably negative everywhere, because the gas density must decline with radius. This scenario, when combined with an initial entropy excess (due to supernova-driven galactic winds, for example), yields an isentropic core that grows as the group evolves. However, the temperature distribution in this preheating scenario is in strong contrast to the data, where, at least within $0.3r_{500}$, the temperature typically exhibits a positive gradient, rising monotonically from the center of groups as well as relaxed rich clusters of galaxies, and declining or remaining constant only outside $0.3r_{500}$ (Pratt & Arnaud 2002; Zhang et al. 2004). Thus there is a fundamental problem with the inner temperature structure predicted by the polytropic preheating models. In the era of ROSAT and ASCA, this disagreement was sometimes explained with the argument that the inner regions of clusters and groups contain cooling flows, which disrupt the equilibrium physics, and which therefore need to be excised (Markevitch 1998) or modeled as two-temperature systems (Ettori 2000). However, Chandra and XMM-Newton show that hydrostatic models—in many cases including the region within the cooling radius—can fit clusters with rising temperature profiles (Schmidt, Allen, & Fabian 2001; Allen, Schmidt, & Fabian 2002; Ettori et al. 2002; Buote et al. 2003; Zhang et al. 2004).

Therefore, rising temperature profiles must be a part of any successful preheating model. The preheating models of Muanwong et al. (2002), Tornatore et al. (2003), and McCarthy et al. (2004), for example, do away with the polytropic assumption, and therefore can reproduce the positive inner temperature gradients observed in many clusters. These works show that when radiative cooling is also included, the models with and without preheating produce nearly indistinguishable radial entropy profiles. In all these calculations, regardless of the treatment of cooling, the large isentropic cores vanish. It is interesting to note that in all cases the non-preheated scenarios provide the

most satisfactory description of the our XMM-Newton data, predicting entropy distributions with slopes close to our observed of $0.92^{+0.04}_{-0.05}$ within $0.3r_{500}$. In contrast, depending on the redshift at which the energy injection occurs, the preheated models predict shallower inner slopes than we observe. Thus the “similarity break” in the cluster luminosity-temperature relation—one of the original motivations for the notion of preheating—continues to elude self-consistent modeling.

The second chief disagreement—the entropy deficit at the outer radii near r_{500} —is more difficult to explain. While it is possible that substructure or superposition with background clusters could cause the deviation from a single power law, we do observe the decrement in groups that show no evidence of irregularity, such as SS2b153, NRGb184 and NGC 1550 (Sun et al. 2003). An understanding of this entropy deficit will likely require higher signal-to-noise data as well as preheating models that more accurately reflect the temperature distribution of the intragroup medium.

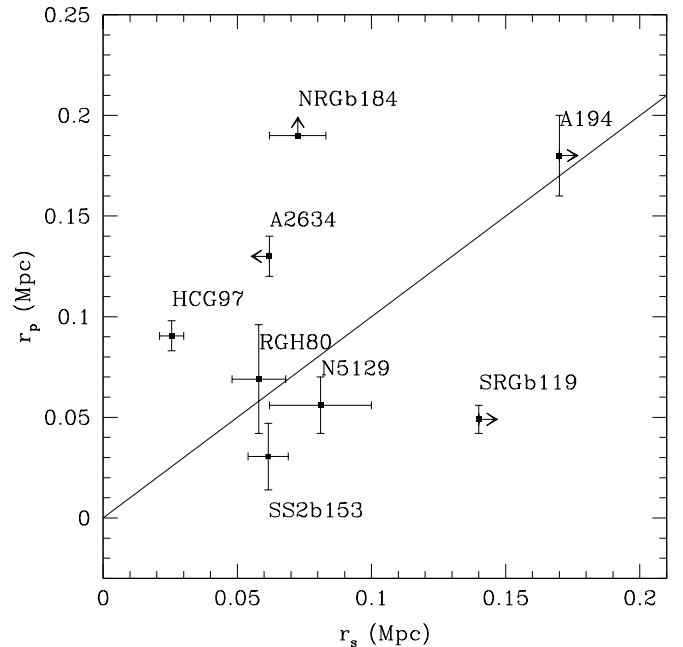


FIG. 8.— The pressure transition slope r_p compared to the entropy transition slope r_s . The solid straight line corresponds to $r_s = r_p$; arrows indicate upper or lower limits.

Returning to the self-similar fits, we briefly comment on the physical significance of the independently derived transition radii r_s and r_p . Because these breaking radii are typically $\gg 10$ kpc, it is unlikely that they are simply related to the effect of the potential of the central galaxy on the gas distribution. Similarly, most of the measured radii are larger than the size of a typical group-scale cooling flow (≈ 20 kpc). Thus, it is more likely that the transition radii are reflective of the properties of the gas distribution throughout the group, rather than just the effect of a central galaxy or cooling flow. In that case, given a perfectly self-similar sample, one would expect a monotonic functional relationship between r_s and r_p : as the entropy

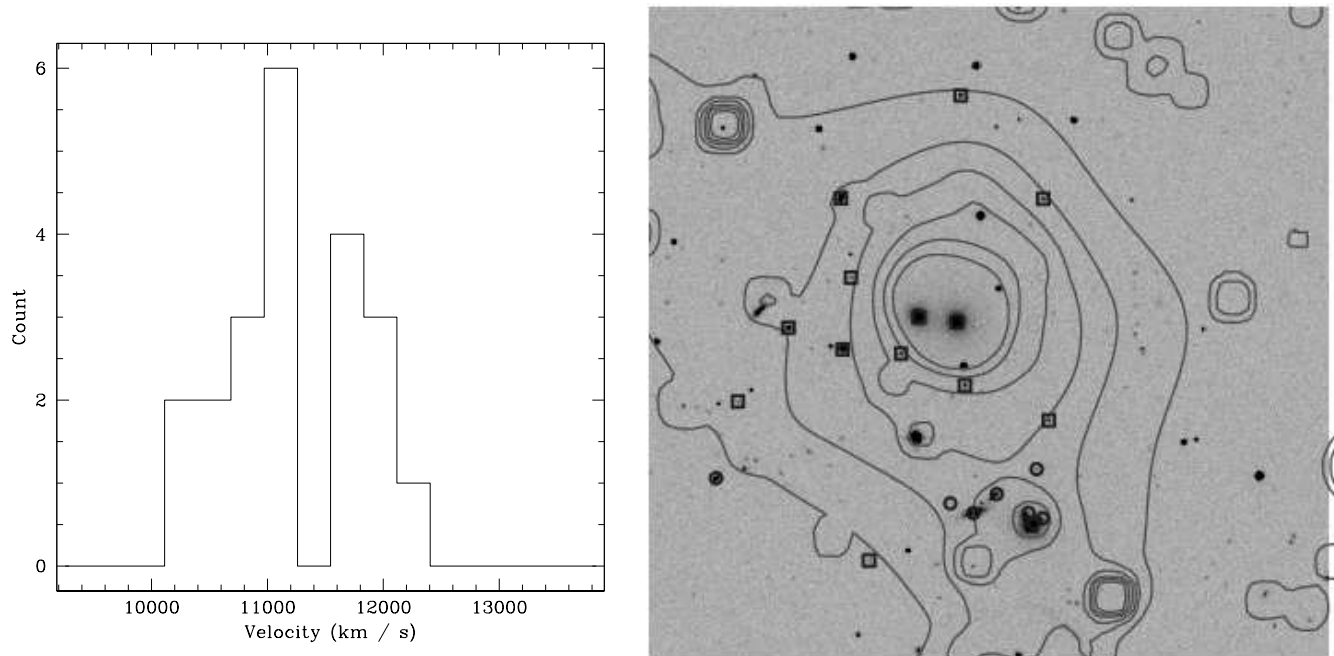


FIG. 9.— (*Left*) Histogram of velocities for galaxies within $12'$ of the center of the RGH 80 group. There is a gap of 490 km s^{-1} between the two peaks, comparable to the group's overall velocity dispersion. (*Right*) POSS image of RGH80, showing galaxies belonging to the histogram's low velocity peak (squares) and high velocity peak (circles). The circles are concentrated around the SW X-ray emission peak.

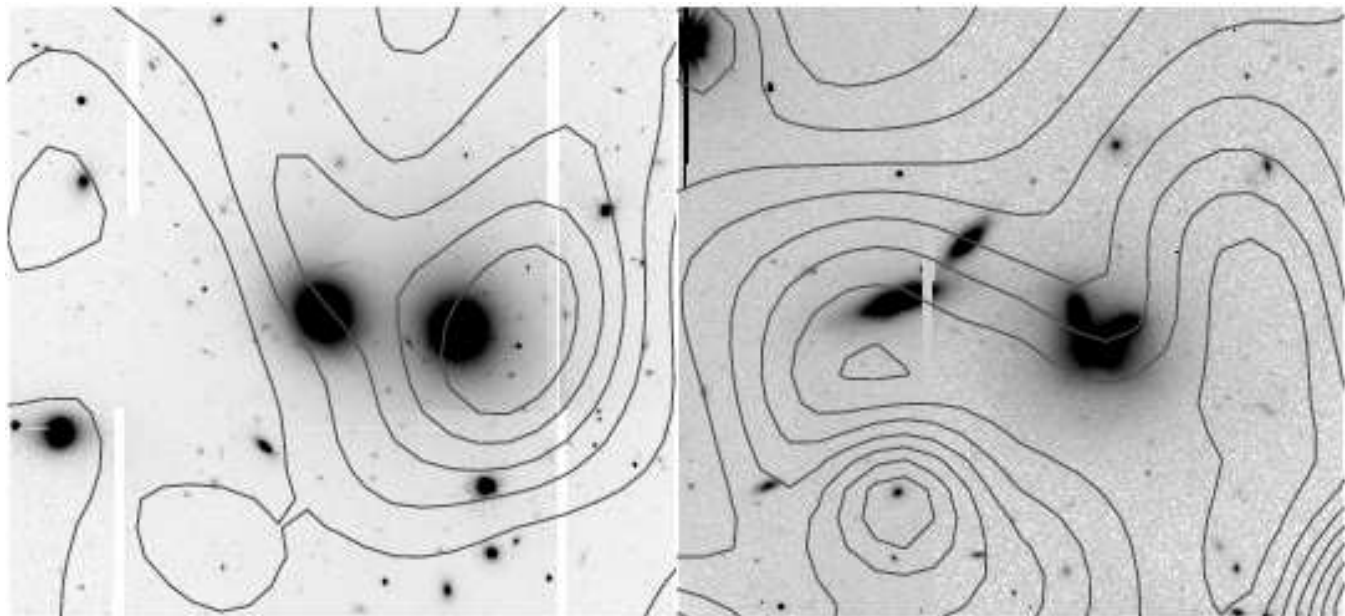


FIG. 10.— *R*-band Gemini GMOS acquisition images of RGH80, showing the dominant X-ray peak (*left*) and the subgroup to the SW (*right*). Also shown are lines of constant emission-weighted temperature. In each case, the innermost contour shows a temperature of 0.6 keV; each larger contour corresponds to an increment of 0.05 keV from the previous one.

transition radius increases or decreases, the pressure radius should follow suit. The simplest such scenario would be $r_s = r_p$, i.e., the entropy and the pressure profiles both breaking at the same point. We examine this possibility in Figure 8. Here we see that half the sample does lie close to the $r_s = r_p$ relationship: RGH 80, NGC 5129, SS2b153, and Abell 194 are within 1σ of the line. Of these, the first three appear relaxed in both their X-ray and optical morphology (see §5 below). Of systems that deviate from the $r_s = r_p$ line, Abell 2634, SRGb119, and HCG 97 show hints of irregularities that we discuss in §5 below, while NRGb184 appears relaxed. Thus the relationship between r_s and r_p is a useful (if not foolproof) tool in evaluating the equilibrium state of a system of galaxies.

Thus the XMM-Newton observations demonstrate that our sample of groups has a self-similar azimuthally averaged pressure distribution. The entropy profiles also appear similar. These entropy profiles have shapes that challenge detailed theoretical models that include preheating (Tozzi et al. 2000; Tozzi & Norman 2001). Furthermore, non-preheated models are valid only in the *inner* regions—we find $S(r) \propto r^{0.91 \pm 0.04}$, closely matching the models' predicted $S(r) \propto r^{1.1}$. However, as our data approaches r_{500} , the slope flattens, even in groups where the gas distribution appears regular. Present preheating models do not account for the $\gamma_s \approx 0.4$ slope we find near r_{500} .

5. PROPERTIES OF INDIVIDUAL SYSTEMS

Before we discuss the properties of the individual systems, the heterogeneous nature of the sample as a whole is worth pointing out. No two systems in our sample resemble one another morphologically. There is a spherical and relaxed-seeming group (SS2b153), a Hickson (1982) compact group merging with a sub-group (HCG 97), an apparent merger that the optical data reveal to be a superposition (RGH 80 and Abell 194), a linear cluster (Abell 194), and three loose groups. These systems are a random and plausibly representative subsample of the optically selected RASSCALs galaxy groups.

5.1. RGH80

This group of galaxies was originally described by Ramella et al. (1989); it was observed by ROSAT as well as ASCA, which yielded spectra with emission-weighted temperatures ≈ 1.5 keV and metallicities ≈ 0.5 solar (Hwang et al. 1999). The XMM observations of this group are described in detail by Xue, Böhringer, & Matsushita (2004), who find that the data are consistent with a monotonically decreasing metallicity distribution.

Our new optical data suggests the presence of a second group in the field of RGH 80. The X-ray peak to the SW of the central peak contains another concentration of galaxies. These galaxies are also distinct from the main peak. Figure 9 shows a histogram of the rest-frame velocities of the galaxies within the central $12'$. The 21 galaxies in this region exhibit a 490 ± 10 km s $^{-1}$ void in velocity space. The centers of the peaks themselves are separated by 1080 ± 103 km s $^{-1}$. If we split the two systems at the midpoint of this void, we see that 7 of the 8 galaxies in the higher-velocity peak reside within $30''$ (20 kpc) of the SW X-ray peak. This lends support to the idea that the SW peak, separated from the main peak by 156 ± 5 kpc, is

a dynamically distinct group of galaxies. The two groups are shown in Figure 10.

Several lines of reasoning suggests that the SW group has not interacted with the main group. The void in the velocity histogram (490 km s $^{-1}$) is comparable to the velocity dispersion of the group overall (≈ 600 km s $^{-1}$). The size of this void argues against a scenario in which the two groups have already interacted. If one group were bound to and had already passed through the other, at least a few galaxies within our detection limit ought to have been displaced to occupy the velocity gap.

We can make this argument more rigorous by examining a two body model first used by Beers, Geller, & Huchra (1982) to study rich clusters of galaxies. In this simplified scenario, the two groups are approximately point masses in an orbit with zero angular momentum. Given a line-of-sight velocity difference and a projected distance between the two bodies, the model allows one to solve for $M(i)$, the total mass required to bind the system as a function of the inclination angle i between the observer's line of sight and the orbital axis. We plot this function in Figure 11. We also show the mass inferred from our temperature measurements via the X-ray mass-temperature relation (Finoguenov, Reiprich, & Böhringer 2001). In the case of RGH 80, the main NE clump has an emission-weighted temperature in the range 0.7–0.9 keV; for the SW clump, the range is 0.5–0.7 keV, corresponding to an estimated mass of $1.8\text{--}3.2 \times 10^{13} M_\odot$ within r_{500} . (68% confidence, taking into account errors in the mass-temperature relation as well as our own measurement errors). To estimate the remaining material within the virial radius r_{200} , we assume that the matter distribution of both clumps can be described by a Navarro et al. (1997) profile with transition radius r_{500} ; we arrived at this value by examining the mass profiles derived in the infall regions of similar systems by Rines et al. (2003), and converting their best-fit NFW profiles to our r_{500} reference frame. The virial mass of the two clumps is then 1.3 times the mass at r_{500} , or $2.3\text{--}4.2 \times 10^{13} M_\odot$. The minimum mass required to bind the group is about 3 times larger than the X-ray mass inferred from the mass-temperature relation. In the context of the simple two-body model, then, it is unlikely that the groups are bound.

The X-ray morphology leads to a similar conclusion. The maps of this region show two distinct entropy minima, with no shocks indicating a merging history. Both the central clump and the southern clump are embedded in separate low-entropy zones. It is more likely that the SW pressure enhancement corresponds to a separate dark matter concentration associated with the potential of the SW group, and less likely that it corresponds to a shock. The spectral fits show that there are two components consistent with being projected on top of each other. In the NE source, we observe a rise of the temperature from 0.9 keV to 1.2 keV, and then in the outer regions back down again to 0.7 keV. The metallicity is enhanced in the SW peak compared to the rest of the image—it is distinct from its surroundings. Thus the X-ray observations also support a scenario in which the SW group is dynamically independent of the rest of the system.

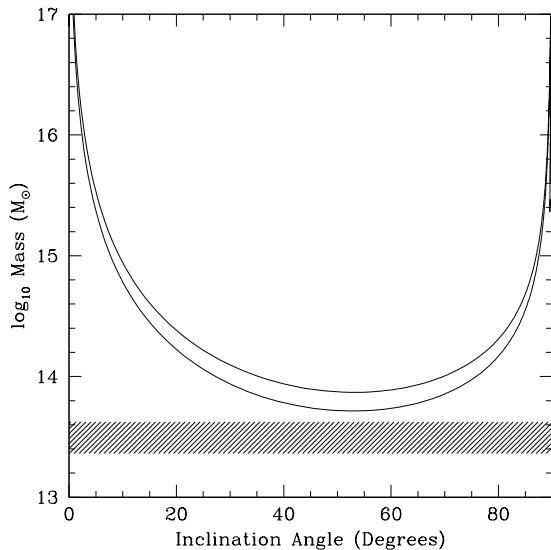


FIG. 11.— Simple two-body analysis of the NE and SW groups in RGH 80. The two solid lines indicate upper and lower limits on the minimum total mass required to bind the two groups to each other. For inclinations $i < 89^\circ$, only incoming bound solutions are possible; for $i > 89^\circ$, both incoming and outgoing bound solutions are possible, but the latter occupy only a minuscule region in the solution space. The lower shaded region indicates the total mass of the system derived from the X-ray mass-temperature relation. The X-ray mass is too small to bind the groups by about a factor of 5.

5.2. *Abell 194*

Abell 194 was originally classified as a “linear” cluster of galaxies by Rood & Sastry (1971) because of its NE-SW alignment. Our XMM-Newton observation shows that the alignment also exists in the X-ray. The first impression is that there are three peaks: one to NE, one in the center, and one to the SW. The X-ray spectrum of the central $15''$ of the NE peak is consistent with that of an active galactic nucleus (AGN).

It is however the southwesternmost X-ray peak that would seem to be of particular interest, because Knezek & Bregman (1998) report that the galaxy at its center has a redshift consistent with that of Abell 194. Yet this galaxy is at least four magnitudes fainter than the galaxies occupying the two other, bright X-ray emission peaks. This would imply an unreasonably large mass-to-light ratio of ≈ 1000 for the SW X-ray peak. Upon reanalyzing the Knezek & Bregman (1998) spectrum (Figure 12), we find that its recession velocity is $47900 \pm 140 \text{ km s}^{-1}$. Also, the X-ray spectrum corresponding to the SW region is better fit by a thermal plasma at redshift 0.15 than it is by a plasma at redshift 0.017. The galaxy atop the SW X-ray peak is therefore the brightest member of a more distant cluster, and the peak is not associated with Abell 194, but corresponds to the X-ray atmosphere of the cluster at $z = 0.15$. This result, together with the result for RGH 80, stresses the importance of projection effects when considering the properties of clusters and groups of galaxies (Cen 1997).

Thus, there are only two distinct halos in Abell 194, both exhibiting an outward rise in temperature from 0.7 keV in the center to 1.6 keV in the outskirts. The velocity distributions of the galaxies within each X-ray peak are indistinguishable; as a result it is likely that the two clumps are bound.

The entropy profile of Abell 194 seems to resist an azimuthally averaged description (§ 4). The cluster registers a larger χ^2 than the other seven systems in our sample, regardless of the entropy model. Given that it is by far the least axisymmetric cluster in our sample, the disagreement is hardly a surprise. However, it is surprising that the pressure profile is fully consistent with the self-similar model fit to the rest of the sample.

5.3. *HCG 97*

HCG 97 is a group of galaxies originally discussed in the Hickson (1982) catalog of compact systems. Ebeling et al. (1994) first reported X-ray emission in the ROSAT All-Sky Survey for this group.

Our analysis of the XMM-Newton observation reveals a complex structure in this interacting system, with a large gas tail stretching toward the SE. This tail is a source of low-entropy gas and may account for the deficit seen in the entropy profile at around $0.5r_{500}$. The Gemini observation reveals a single member galaxy inhabiting the SE extension plume; a close examination of the GMOS acquisition image (Figure 13) reveals no background clusters that could be responsible for the X-ray emission in that region.

If the SE plume is associated with the cluster, it may be a relic of the infall of one of the brighter interacting galaxies at the group center—or it may be yet another chance superposition from a cluster not visible in the Gemini image. The temperature of the plume is consistent with that of its surroundings; i.e., the plume is not apparent in the temperature map (Figure 4). However, the plume is clearly present in the entropy, pressure, and density distributions. Neither the X-ray and the optical data are at this point of sufficient quality to determine whether the plume has been stripped from one of the central galaxies, or whether it is a background structure unrelated to the main group.

Substructure notwithstanding, the azimuthally averaged pressure and entropy distributions in HCG 97 are consistent with the self-similar power laws fitted to the sample as a whole.

5.4. *SS2b153*

SS2b153 is a remarkably round system, a stark contrast to the complexity of the other groups. Because the only redshifts available in its region are from the nearly decade-old Las Campanas Redshift Survey (Shectman et al. 1996), very few galaxies are known to be members.

The azimuthally averaged pressure and entropy distributions in this system are consistent with the self-similar broken power law fit to the sample as a whole, except for the innermost data point. The pressure at $\approx 10 \text{ kpc}$ disagrees with the self-similar law by a factor of 2. SS2b153 is the most nearby group in the sample, and it is possible that the pressure enhancement represents the contribution of the gas bound to the central galaxy, NGC 3411, to the total pressure. Similar enhancements—associated with the central galaxies of groups within $z \approx 0.01$ —have been observed in other systems (Helsdon et al. 2001).

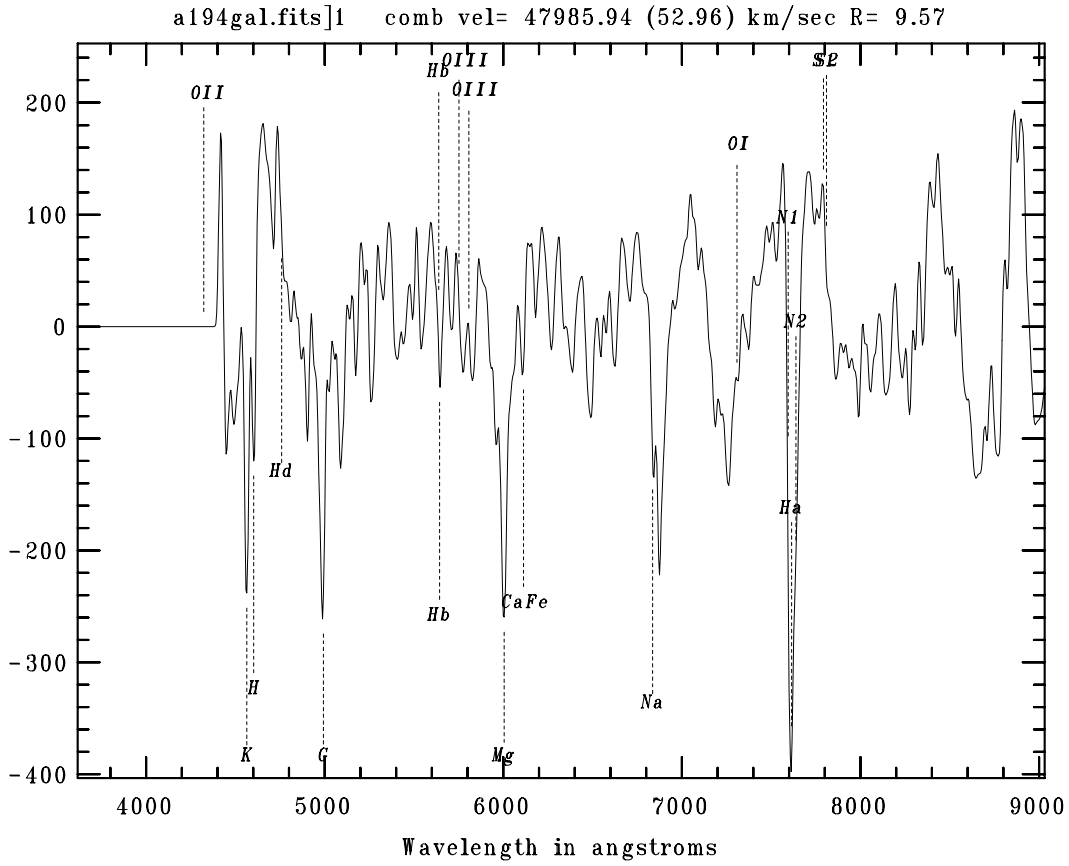


FIG. 12.— Continuum-subtracted spectrum of the galaxy associated with the SW emission peak in the XMM-Newton observation of Abell 194. The redshift of the galaxy indicates that it is a distant background cluster, and not related to Abell 194.

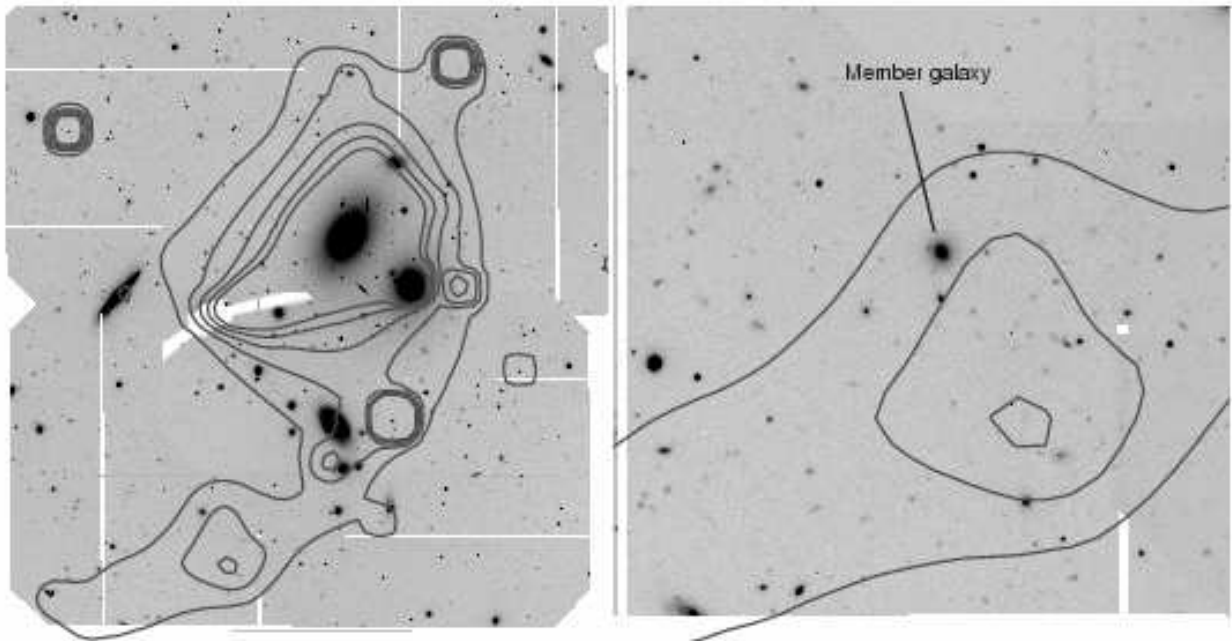


FIG. 13.— (left) A 10 minute, *R* band Gemini GMOS acquisition image of HCG 97. X-ray surface brightness contours from our wavelet decomposition technique are superimposed. The plume to the SE (right) is coincident with a single member galaxy. There are no noticeable background clusters associated with the peak within the SE extension.

5.5. NGC 5129 Group

The “plume” to the NE seems to be indistinguishable from its environment to within the errors. The entire central region seems roughly isothermal, with a temperature 0.7 keV. The entropy profile of the NGC 5129 Group does not reveal any deviations from the self-similar models, and its pressure profile also appears consistent.

5.6. Abell 2634

The XMM-Newton observation of Abell 2634 was plagued by long periods of high X-ray background, which did not allow us to extract as much spectroscopic information as would have otherwise been possible for this bright cluster. The radio source 3C 465 coincides with the central galaxy (Owen & Rudnick 1976; Sakelliou & Merrifield 1999); it exhibits a powerful jet that interacts the X-ray emitting gas as far out as 100 kpc from the cluster center. For this reason, our entropy and pressure profiles miss the central section of the cluster entirely.

5.7. NRGb184

The group has a north/south elongation in surface brightness. This elongation is less pronounced in the pressure map. There is a $\sim 20\%$ pressure difference between the regions directly to the SE and NW of the group center. The temperature rises fairly quickly from 0.6 keV in the very central region to about 1.5 keV. The N-S extension that is visible in the surface brightness map is not present in temperature map. On both the entropy and pressure plots, the properties of the gas in NRGb184 appear typical.

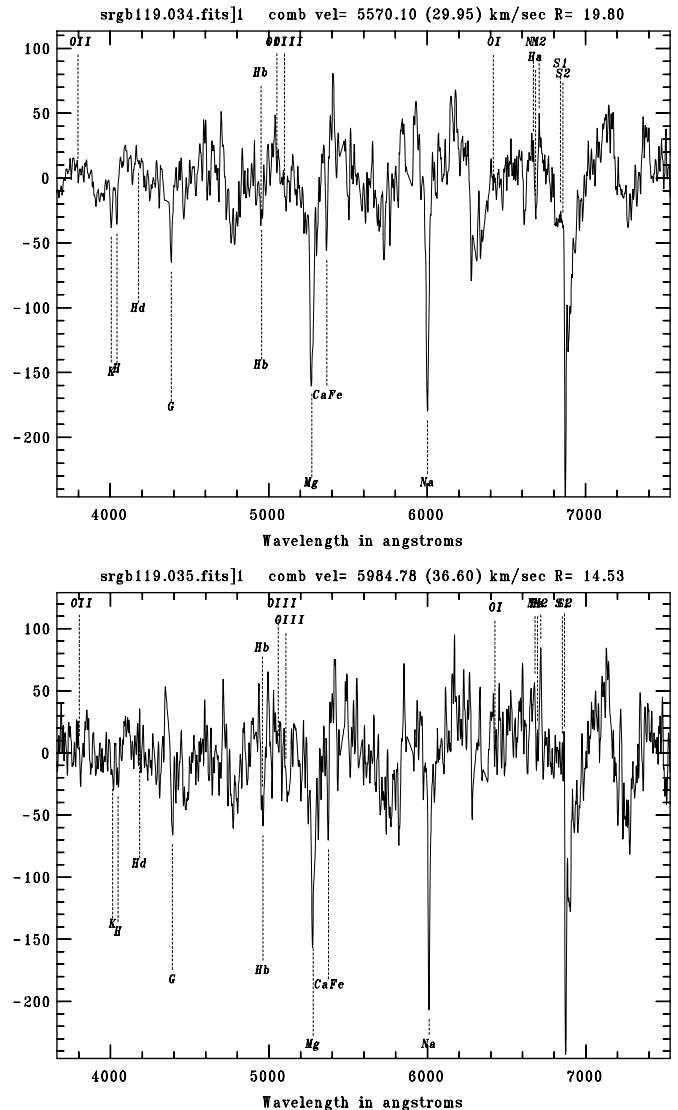


FIG. 14.— Continuum-subtracted spectra of the western (*top*) and eastern (*bottom*) pair of central galaxies in SRGb119. .

5.8. SRGb119

In general, the temperature increases from 0.7 keV towards the center to 1.4 keV towards the exterior. There are too few counts to constrain the iron abundance robustly. – There is an interesting unresolved source to the east of the very center of the group. It is a member galaxy that is ~ 2 mag fainter than the brightest group galaxy. The two galaxies have a large velocity difference (450 km s^{-1}). Despite being fainter, the galaxy to the E has a higher temperature than the central source, $1.6 \pm 0.2 \text{ keV}$ compared to $0.7 \pm 0.2 \text{ keV}$. The optical spectra of both the central galaxies show no evidence of AGN emission (Figure 14). The higher X-ray temperature for the source to the east is therefore a puzzle. Our analysis rules out a significant contribution coming from low-mass X-ray binaries (LMXBs): the spectrum is inconsistent with the $\gtrsim 5$ keV temperatures expected from these objects (Sarazin, Irwin, & Bregman 2001). At the same time, however, a power law spectrum with index 2.9 ± 0.4 provides a better fit than a thermal plasma. The power law spectrum has a total luminosity of $9 \times 10^{40} \text{ ergs/s}$ in the 0.5–2 keV band.

The source of this spectrum could be a veiled AGN such as the one observed in NGC 1291 by Irwin, Sarazin, & Bregman (2002).

The pressure and entropy distribution in SRGb119 presents a puzzle similar to that of Abell 194. By itself, the azimuthally averaged entropy profile of SRGb119 is not a good fit to the simple empirical models in §4. Of the eight groups in our sample, SRGb119 makes the second largest contribution to the reduced χ^2 (after Abell 194), regardless of the shape of the model. However, similarly to Abell 194, SRGb119 is quite consistent with the self-similar pressure models. Thus we find that the two groups with the more discrepant entropy distributions are nevertheless similar to the rest of the sample when we consider the pressure profiles.

6. CONCLUSION

We use new and previously unpublished archival XMM-Newton data to examine the properties of the X-ray emitting medium in eight groups of galaxies from the RASS-CALS survey. In addition to the X-ray data, we collect redshifts for the group members from the literature. We also report redshifts from a Gemini North Observatory survey of the groups RGH 80, HCG 97, and NRGb184.

The sample consists of groups with X-ray luminosities $\lesssim 10^{43}$ erg s $^{-1}$, and was chosen based on availability in the XMM-Newton data archive. The groups in the sample exhibit a wide variety of X-ray and optical morphologies, from seemingly perfectly spherical systems (SS2b153) to linear clusters (Abell 194). Many of the systems exhibit certain or possible superposition, in both the X-ray and optical, with unrelated background galaxies or clusters of galaxies. We use the Gemini North optical data to argue that RGH 80 is a superposition of two dynamically unrelated groups.

Despite the morphological incongruity of the groups, they exhibit regularity in their azimuthally averaged pressure and entropy profiles. Self-similar broken power laws can describe the spatial distribution of both these quantities. For the entropy, which increases with distance from the center, we find an inner slope $\alpha_s = 0.92^{+0.04}_{-0.05}$ and outer slope $\gamma_s = 0.42^{+0.05}_{-0.04}$ (68% confidence). These results argue against the existence of an isentropic “floor” at the center of X-ray emitting groups, and against theoretical models that describe the entropy distribution as a single power law for $r \gtrsim 0.3r_{500}$.

The decreasing pressure profiles are also well-fitted by a self-similar broken power law. The inner and the outer slopes are $\alpha_p = -0.78^{+0.04}_{-0.03}$ and $\gamma_p = -1.7^{+0.1}_{-0.3}$ for the entire sample. The regularity and similarity of the pressure profiles suggests that the groups reside in dark matter halos that are similar in structure.

We have made use of the NASA/IPAC Extragalactic Database (NED) which is operated by the Jet Propulsion Laboratory, California Institute of Technology, under contract with the National Aeronautics and Space Administration. We thank Patricia Knezeck for providing us with the spectrum of the galaxy in the SW X-ray peak in Abell 194, and the anonymous referee for comments that improved the paper. J. P. H. thanks the Alexander von Humboldt Foundation for support in Garching. M. J. G. was supported by the Smithsonian Institution. A. F. acknowledges support from BMBF/DLR under grant 50 OR 0207, from MPG, and from NASA grant NNG04GH226. A. M. was supported by NASA through a Chandra Postdoctoral Fellowship Award issued by the Chandra X-ray Observatory Center, which is operated by the Smithsonian Astrophysical Observatory for and on behalf of NASA under contract NAS 8-39073.

REFERENCES

- Abazajian, K., Adelman-McCarthy, J. K., Agüeros, M. A., Allam, S. S., Anderson, K. S. J., Anderson, S. F., Annis, J., Bahcall, N. A., et al. 2004, *AJ*, 128, 502
- Allen, S. W., Schmidt, R. W., & Fabian, A. C. 2002, *MNRAS*, 335, 256
- Anders, E. & Grevesse, N. 1989, *Geochim. Cosmochim. Acta*, 53, 197
- Beers, T. C., Geller, M. J., & Huchra, J. P. 1982, *ApJ*, 257, 23
- Bertin, E. & Arnouts, S. 1996, *A&AS*, 117, 393
- Buote, D. A., Lewis, A. D., Brighenti, F., & Mathews, W. G. 2003, *ApJ*, 594, 741
- Cen, R. 1997, *ApJ*, 485, 39
- Danese, L., de Zotti, G., & di Tullio, G. 1980, *A&A*, 82, 322
- Diaferio, A., Ramella, M., Geller, M. J., & Ferrari, A. 1993, *AJ*, 105, 2035
- Dickey, J. M. & Lockman, F. J. 1990, *ARA&A*, 28, 215
- Dos Santos, S. & Doré, O. 2002, *A&A*, 383, 450
- Ebeling, H., Voges, W., & Böhringer, H. 1994, *ApJ*, 436, 44
- Ettori, S. 2000, *MNRAS*, 318, 1041
- Ettori, S., Fabian, A. C., Allen, S. W., & Johnstone, R. M. 2002, *MNRAS*, 331, 635
- Finoguenov, A., Borgani, S., Tornatore, L., & Böhringer, H. 2003, *A&A*, 398, L35
- Finoguenov, A., Jones, C., Böhringer, H., & Ponman, T. J. 2002, *ApJ*, 578, 74
- Finoguenov, A., Pietsch, W., Aschenbach, B., & Miniati, F. 2004, *A&A*, 415, 415
- Finoguenov, A., Reiprich, T. H., & Böhringer, H. 2001, *A&A*, 368, 749
- Geller, M. J. & Huchra, J. P. 1983, *ApJS*, 52, 61
- Ghigna, S., Moore, B., Governato, F., Lake, G., Quinn, T., & Stadel, J. 2000, *ApJ*, 544, 616
- Helsdon, S. F. & Ponman, T. J. 2000, *MNRAS*, 315, 356
- Helsdon, S. F., Ponman, T. J., O’Sullivan, E., & Forbes, D. A. 2001, *MNRAS*, 325, 693
- Henry, J. P., Finoguenov, A., & Briel, U. G. 2004, *ApJ*, 615, 181
- Hickson, P. 1982, *ApJ*, 255, 382
- Hwang, U., Mushotzky, R. F., Burns, J. O., Fukazawa, Y., & White, R. A. 1999, *ApJ*, 516, 604
- Ikebe, Y., Reiprich, T. H., Böhringer, H., Tanaka, Y., & Kitayama, T. 2002, *A&A*, 383, 773
- Irwin, J. A., Sarazin, C. L., & Bregman, J. N. 2002, *ApJ*, 570, 152
- Knezeck, P. M. & Bregman, J. N. 1998, *AJ*, 115, 1737
- Kurtz, M. J. & Mink, D. J. 1998, *PASP*, 110, 934
- Lewis, A. D., Buote, D. A., & Stocke, J. T. 2003, *ApJ*, 586, 135
- Lin, Y., Mohr, J. J., & Stanford, S. A. 2004, *ApJ*, 610, 745
- Lloyd-Davies, E. J., Ponman, T. J., & Cannon, D. B. 2000, *MNRAS*, 315, 689
- Loewenstein, M. 2001, *ApJ*, 557, 573
- Lumb, D. H., Bartlett, J. G., Romer, A. K., Blanchard, A., Burke, D. J., Collins, C. A., Nichol, R. C., Giard, M., et al. 2004, *A&A*, 420, 853
- Lupton, R. 1993, *Statistics in theory and practice* (Princeton, N.J.: Princeton University Press, —c1993)
- Mahdavi, A., Böhringer, H., Geller, M. J., & Ramella, M. 2000, *ApJ*, 534, 114
- Mahdavi, A. & Geller, M. J. 2004, *ApJ* in press (astro-ph/0402161)
- Mahdavi, A., Geller, M. J., Böhringer, H., Kurtz, M. J., & Ramella, M. 1999, *ApJ*, 518, 69
- Markevitch, M. 1998, *ApJ*, 504, 27
- McCarthy, I. G., Balogh, M. L., Babul, A., Poole, G. B., & Horner, D. J. 2004, *ApJ*, 613, 811
- Metzler, C. A. & Evrard, A. E. 1994, *ApJ*, 437, 564
- Muanwong, O., Thomas, P. A., Kay, S. T., & Pearce, F. R. 2002, *MNRAS*, 336, 527
- Mulchaey, J. S. 2000, *ARA&A*, 38, 289

- Navarro, J. F., Frenk, C. S., & White, S. D. M. 1997, *ApJ*, 490, 493
 Owen, F. N. & Rudnick, L. 1976, *ApJ*, 205, L1
 Pinkney, J., Rhee, G., Burns, J. O., Hill, J. M., Oegerle, W., Batuski, D., & Hintzen, P. 1993, *ApJ*, 416, 36
 Ponman, T. J., Bourner, P. D. J., Ebeling, H., & Bohringer, H. 1996, *MNRAS*, 283, 690
 Ponman, T. J., Cannon, D. B., & Navarro, J. F. 1999, *Nature*, 397, 135
 Ponman, T. J., Sanderson, A. J. R., & Finoguenov, A. 2003, *MNRAS*, 343, 331
 Pratt, G. W. & Arnaud, M. 2002, *A&A*, 394, 375
 Press, W. H., Teukolsky, S. A., Vetterling, W. T., & Flannery, B. P. 1992, *Numerical recipes in FORTRAN. The art of scientific computing* (Cambridge: University Press, —c1992, 2nd ed.)
 Ramella, M., Diaferio, A., Geller, M. J., & Huchra, J. P. 1994, *AJ*, 107, 1623
 Ramella, M., Geller, M. J., & Huchra, J. P. 1989, *ApJ*, 344, 57
 Ramella, M., Geller, M. J., Pisani, A., & da Costa, L. N. 2002, *AJ*, 123, 2976
 Reiprich, T. H. & Böhringer, H. 2002, *ApJ*, 567, 716
 Rines, K., Geller, M. J., Kurtz, M. J., & Diaferio, A. 2003, *AJ*, 126, 2152
 Rood, H. J. & Sastry, G. N. 1971, *PASP*, 83, 313
 Sakelliou, I. & Merrifield, M. R. 1999, *MNRAS*, 305, 417
 Sanderson, A. J. R., Ponman, T. J., Finoguenov, A., Lloyd-Davies, E. J., & Markevitch, M. 2003, *MNRAS*, 340, 989
 Sarazin, C. L., Irwin, J. A., & Bregman, J. N. 2001, *ApJ*, 556, 533
 Schmidt, R. W., Allen, S. W., & Fabian, A. C. 2001, *MNRAS*, 327, 1057
 Shectman, S. A., Landy, S. D., Oemler, A., Tucker, D. L., Lin, H., Kirshner, R. P., & Schechter, P. L. 1996, *ApJ*, 470, 172
 Sun, M., Forman, W., Vikhlinin, A., Hornstrup, A., Jones, C., & Murray, S. S. 2003, *ApJ*, 598, 250
 —. 2004, *ApJ*, 612, 805
 Tonry, J. & Davis, M. 1979, *AJ*, 84, 1511
 Tornatore, L., Borgani, S., Springel, V., Matteucci, F., Menci, N., & Murante, G. 2003, *MNRAS*, 342, 1025
 Tozzi, P. & Norman, C. 2001, *ApJ*, 546, 63
 Tozzi, P., Scharf, C., & Norman, C. 2000, *ApJ*, 542, 106
 Vikhlinin, A., McNamara, B. R., Forman, W., Jones, C., Quintana, H., & Hornstrup, A. 1998, *ApJ*, 502, 558
 Voit, G. M. & Ponman, T. J. 2003, *ApJ*, 594, L75
 White, R., Bliton, M., Bhavsar, S. P., Suketu, P., Bornmann, P., Burns, J. O., Ledlow, M. J., & Loken, C. 1999, *AJ*, 118, 2014
 Xue, Y.-J., Böhringer, H., & Matsushita, K. 2004, *A&A*, 420, 833
 Zabludoff, A. I., Huchra, J. P., & Geller, M. J. 1990, *ApJS*, 74, 1
 Zabludoff, A. I. & Mulchaey, J. S. 1998, *ApJ*, 496, 39
 Zhang, Y.-Y., Finoguenov, A., Böhringer, H., Ikebe, Y., Matsushita, K., & Schuecker, P. 2004, *A&A*, 413, 49
 Zwicky, F. 1937, *ApJ*, 86, 217
 Zwicky, F. & Humason, M. L. 1960, *ApJ*, 132, 627

TABLE 1
 GROUP SAMPLE

Primary ID	α_{2000}	δ_{2000}	N	$c\bar{z}$	σ_{1os}	Other ID	Central Galaxy	Sources
Abell 194	01:25:48.1	-01:23:06	106	5316^{+53}_{-53}	550^{+89}_{-86}	SRGb103	^a	R(106)
SRGb119	01:56:20.8	+05:37:40	61	5525^{+52}_{-48}	416^{+34}_{-33}	WBL 61	NGC 741	M(21), Z(30)
SS2b153	10:50:26.3	-12:50:43	5	4747^{+59}_{-69}	161^{+19}_{-71}	USGC S152	NGC 3411	L(14)
NRGb184	12:08:05.5	+25:14:14	33	6700^{+46}_{-62}	390^{+40}_{-37}	...	UGC 07115	G(8), M(52)
RGH80	13:20:14.8	+33:08:35	58	11047^{+74}_{-80}	602^{+63}_{-61}	NRGs241	NGC 5098	G(14), M(44)
NGC 5129	13:24:09.6	+13:58:51	33	6952^{+46}_{-44}	283^{+29}_{-31}	NRGb244	NGC 5129	M(19), Z(15)
Abell 2634	23:38:29.2	+27:01:54	69	9391^{+73}_{-72}	568^{+39}_{-43}	3C 465 / SRGs040	NGC 7720	P(69)
HCG 97	23:47:23.1	-02:18:07	37	6758^{+62}_{-49}	383^{+50}_{-52}	SS2b312	IC 5357	G(11), M(26)

Note. — N is the number of known members within 2 Mpc of the X-ray center of the group; $c\bar{z}$ is the mean redshift of the group multiplied by the speed of light in km s^{-1} ; σ_{1os} is the velocity dispersion of the group in km s^{-1} . Also shown are other names of each group, as well as the common name of the central galaxy. The redshifts are taken from the following sources: Mahdavi & Geller (2004, M); Shectman et al. (1996, L); Zabludoff & Mulchaey (1998, Z); Ramella et al. (2002, U); Rines et al. (2003, R); Pinkney et al. (1993, P); and Gemini (G) redshifts measured in this work. The number after each letter indicates the number of unique galaxies that were measured in that work.

^aThe “chain cluster” Abell 194 does not have a dominant galaxy.

TABLE 2
NEW OPTICAL DATA

α_{2000}	δ_{2000}	cz	ϵ_{cz}	Type ^a
12:07:44.31	+25:14:48.5	41241	8	E
12:07:45.67	+25:14:36.9	26338	5	E
12:07:46.99	+25:15:51.5	6468	16	A
12:07:47.71	+25:11:13.2	62187	102	A
12:07:49.53	+25:12:35.9	29447	9	E
12:07:54.08	+25:16:58.9	155457	22	E
12:07:55.33	+25:14:00.2	89416	30	A
12:07:57.64	+25:16:43.3	126564	12	E
12:07:58.16	+25:10:17.8	112008	38	A
12:07:59.33	+25:11:45.9	5896	59	A
12:08:00.12	+25:15:14.9	85701	25	E
12:08:01.94	+25:15:43.3	100206	40	A
12:08:02.23	+25:11:18.2	7096	36	A
12:08:04.01	+25:16:30.1	134066	36	A
12:08:04.68	+25:19:10.0	142108	24	E
12:08:06.12	+25:16:02.9	5813	23	A
12:08:06.23	+25:13:31.6	160608	44	A
12:08:07.16	+25:15:36.9	6502	19	A
12:08:07.44	+25:12:51.5	6964	38	A
12:08:08.16	+25:14:44.3	89252	22	A
12:08:08.86	+25:13:05.2	25449	19	A
12:08:10.42	+25:16:03.3	197516	30	E
12:08:11.97	+25:11:21.9	24130	12	E
12:08:12.37	+25:18:04.3	189232	42	E
12:08:13.18	+25:15:40.3	92668	46	A
12:08:14.87	+25:09:38.8	153102	27	E
12:08:15.42	+25:13:23.3	155169	31	E
12:08:15.86	+25:16:18.6	79235	14	E
12:08:17.88	+25:14:32.2	78955	16	E
12:08:18.85	+25:13:46.3	78683	9	E
12:08:19.19	+25:15:47.2	189886	34	E
12:08:19.37	+25:13:57.9	6912	60	A
12:08:21.44	+25:09:40.9	110299	14	E
12:08:22.19	+25:17:58.6	25738	13	E
12:08:22.26	+25:18:57.8	6827	26	A
12:08:22.88	+25:09:48.9	110235	17	E
12:08:25.33	+25:16:20.9	78222	15	E
13:20:00.91	+33:09:11.9	129328	61	A
13:20:07.44	+33:07:00.8	10991	60	A
13:20:08.12	+33:10:38.0	10999	29	A
13:20:08.32	+33:06:13.0	12317	55	A
13:20:14.00	+33:07:34.0	10483	51	A
13:20:14.70	+33:12:17.6	10594	27	A
13:20:15.01	+33:05:38.1	11922	6	E
13:20:15.05	+33:11:57.3	67931	28	E
13:20:15.99	+33:04:38.3	29945	11	E
13:20:17.45	+33:08:54.4	80238	81	A
13:20:17.76	+33:12:12.1	35837	10	E

TABLE 2—*Continued*

α_{2000}	δ_{2000}	cz	ϵ_{cz}	Type ^a
13:20:18.79	+33:10:17.9	105272	67	A
13:20:18.80	+33:09:55.0	104821	12	E
13:20:19.03	+33:08:03.9	10725	33	A
13:20:20.01	+33:13:30.1	11005	14	E
13:20:21.27	+33:04:41.0	10283	6	E
13:20:23.04	+33:09:17.5	11001	65	A
13:20:23.59	+33:06:40.3	98242	34	A
13:20:25.40	+33:11:24.2	5460	20	E
13:20:27.84	+33:08:27.4	10735	27	A
13:20:31.15	+33:06:08.8	68601	29	A
13:20:31.69	+33:07:14.3	11008	62	A
13:20:33.30	+33:05:59.0	11714	5	E
13:20:33.40	+33:12:00.0	141341	29	E
13:20:35.19	+33:05:40.7	133709	41	E
13:20:36.30	+33:09:45.0	20144	17	E
23:47:05.53	-02:14:30.6	42715	4	E
23:47:06.20	-02:14:10.4	35609	21	E
23:47:09.34	-02:15:37.6	7568	48	A
23:47:09.37	-02:22:40.8	89460	22	E
23:47:09.92	-02:18:54.8	140450	18	E
23:47:10.10	-02:15:11.8	7591	6	E
23:47:10.65	-02:19:38.7	116770	23	E
23:47:11.65	-02:22:34.3	152617	46	A
23:47:14.70	-02:21:53.4	45685	14	E
23:47:15.40	-02:21:35.5	115631	54	A
23:47:15.60	-02:20:50.4	115784	25	A
23:47:16.20	-02:19:09.0	96754	7	E
23:47:18.90	-02:24:12.8	77719	10	E
23:47:19.40	-02:21:19.0	89411	26	E
23:47:19.90	-02:16:50.4	6665	24	A
23:47:19.94	-02:16:34.0	63146	14	E
23:47:20.10	-02:18:37.6	88188	25	A
23:47:20.30	-02:22:26.8	7247	4	E
23:47:20.94	-02:17:32.5	124893	24	E
23:47:21.00	-02:19:28.5	140106	32	E
23:47:21.70	-02:17:32.2	29293	11	E
23:47:22.00	-02:18:53.4	29389	53	A
23:47:22.00	-02:21:12.6	6033	48	A
23:47:22.62	-02:18:14.6	68783	39	A
23:47:22.80	-02:15:25.0	88275	30	A
23:47:23.30	-02:21:47.0	5991	7	E
23:47:23.88	-02:16:02.6	111777	28	E
23:47:24.72	-02:16:35.6	152587	14	E
23:47:24.96	-02:16:24.1	124710	38	A
23:47:25.00	-02:19:35.5	5837	37	A
23:47:26.32	-02:16:44.4	55222	8	E
23:47:26.60	-02:21:11.7	6778	36	A
23:47:26.60	-02:21:11.8	6519	25	E

TABLE 2—*Continued*

α_{2000}	δ_{2000}	cz	ϵ_{cz}	Type ^a
23:47:26.60	-02:21:11.8	6698	6	E
23:47:27.36	-02:17:22.9	169001	32	E
23:47:28.36	-02:24:00.3	169622	27	A
23:47:28.81	-02:20:12.7	-117	45	A
23:47:29.50	-02:18:04.8	68533	16	E
23:47:29.50	-02:18:05.0	68523	12	E
23:47:29.60	-02:22:56.3	169789	5	E
23:47:30.00	-02:23:30.8	41439	13	E
23:47:30.23	-02:16:51.4	125224	26	A
23:47:30.50	-02:22:01.6	168233	30	E
23:47:30.80	-02:19:08.3	45611	30	A
23:47:31.20	-02:20:28.2	42185	8	E
23:47:31.20	-02:20:28.2	42206	45	A
23:47:32.10	-02:18:18.3	72077	16	E
23:47:32.40	-02:22:29.3	6879	66	A
23:47:32.47	-02:16:24.8	115977	39	A
23:47:34.65	-02:18:48.5	185245	28	E
23:47:35.20	-02:21:39.1	84656	17	E
23:47:35.74	-02:15:30.1	135273	37	E
23:47:36.00	-02:24:10.7	129738	26	A
23:47:36.83	-02:17:13.0	69053	9	E
23:47:38.20	-02:20:38.0	183269	24	E
23:47:38.47	-02:16:28.4	106316	28	E
23:47:39.27	-02:14:38.2	169012	10	E
23:47:40.04	-02:18:57.9	139059	11	E
23:47:40.90	-02:21:01.5	68338	12	E
23:47:42.40	-02:23:47.5	66326	19	E
23:47:42.64	-02:14:33.1	115187	21	A
23:47:42.70	-02:21:51.2	129539	42	A
23:47:43.80	-02:17:49.6	138877	21	E

Note. — cz denotes the redshift of the object multiplied by the speed of light; ϵ_{cz} is the 1σ uncertainty in cz ; “type” indicates whether the dominant features in the spectrum are absorption (“A”) or emission (“E”) lines.

TABLE 3
XMM OBSERVATIONAL INFORMATION

Name	Obs. ID	net exp ksec	filter	Orbit	frame time ms
Abell 194	0136340101	12.9	Thin	557	73
SRGb119	0153030701	3.9	Thin	745	73
SS2b153	0146510301	18.5	Thin	555	73
NRGb184	0151400201	8.6	Thin	634	73
RGH 80	0105860101	26.2	Thin	563	199
NGC 5129	0108860701	12.4	Medium	472	73
Abell 2634	0002960101	4.0	Medium	464	73
HCG 97	0152860101	20.9	Thin	559	73

TABLE 4
IGM PROPERTIES OF THE GROUPS BETWEEN $0.1 - 0.5r_{500}$.

Group	r_{500} kpc	$\langle kT \rangle$ keV	$\langle Z \rangle$ Z_{\odot}	$\langle S \rangle$ keV cm ²	$\langle P \rangle$ 10^{-12} ergs cm ⁻³
Abell 194	521	1.36 ± 0.04	0.19 ± 0.03	$260. \pm 15.1$	0.89 ± 0.06
SRGb119	520	1.36 ± 0.07	0.55 ± 0.27	$402. \pm 98.7$	0.46 ± 0.13
SS2b153	407	0.65 ± 0.02	0.15 ± 0.01	$109. \pm 6.8$	0.47 ± 0.03
NRGb184	488	1.26 ± 0.07	0.07 ± 0.02	$192. \pm 13.0$	1.11 ± 0.09
RGH 80	455	1.04 ± 0.02	0.16 ± 0.02	$107. \pm 6.1$	1.67 ± 0.10
NGC 5129	434	0.95 ± 0.05	0.39 ± 0.12	$178. \pm 26.2$	0.60 ± 0.13
Abell 2634	639	2.07 ± 0.11	0.20 ± 0.05	$259. \pm 16.3$	2.42 ± 0.16
HCG 97	420	0.89 ± 0.02	0.17 ± 0.03	$129. \pm 8.6$	0.79 ± 0.06

TABLE 5
SELF-SIMILAR PRESSURE AND ENTROPY PROFILE FITS

Entropy Fits		Pressure Fit	
Entire Sample			
Goodness-of-fit	0.0095 ($\chi^2/\nu = 93/62$)		0.15 ($\chi^2/\nu = 73/62$)
α_s	0.87–0.96	$-\alpha_p$	0.75–0.82
γ_s	0.38–0.47	$-\gamma_p$	1.4–1.8
Abell 194			
r_s	> 0.17	r_p	0.16–0.20
S_0	120–140	P_0	17–20
SRGb119			
r_s	> 0.14	r_p	0.042–0.056
S_0	150–190	P_0	17–26
SS2b153			
r_s	0.054–0.069	r_p	0.014–0.047
S_0	100–120	P_0	19–23
NRGb184			
r_s	0.062–0.083	r_p	> 0.19
S_0	170–200	P_0	12–15
NGC 5129			
r_s	0.062–0.10	r_p	0.042–0.070
S_0	160–200	P_0	11–14
RGH 80			
r_s	0.048–0.068	r_p	0.042–0.096
S_0	110–130	P_0	26–31
Abell 2634			
r_s	< 0.062	r_p	0.12–0.14
S_0	240–600	P_0	75–96
HCG 97			
r_s	0.021–0.030	r_p	0.083–0.098
S_0	180–250	P_0	14–16

Note. — the 68% confidence intervals take into account correlations with all the other parameters. The transition radii r_s and r_p are in units of Mpc; S_0 is in units of keV cm², and P_0 is in units of 10^{-12} erg cm⁻³.